The Arctic Weather Satellite, introducing the sub-millimetre wavelength range for operational ice hydrometeor retrievals

Peter McEvoy[1], Eleanor May[1], and Patrick Eriksson[1]

[1]Department of Environmental and Energy Sciences, Chalmers University of Technology, Gothenburg, Sweden

Correspondence: Peter McEvoy (peter.mcevoy@chalmers.se)

Abstract. The first cloud property retrievals based on operational sub-millimetre measurements are presented, using the channels between 89 and 325 GHz of the Arctic Weather Satellite (AWS). The dataset, designated CHIP-AWS, contains frozen water path (FWP) and the associated mass-weighted mean altitudes and particle sizes. In this first version, results are restricted to latitudes between 60° S and 60° N. The retrievals are based on detailed radiative transfer simulations of instrument observations, informed by ERA5 and CloudSat radar reflectivities, using multiple combinations of hydrometeor habits and particle size distribution models. The actual inversion is made by a quantile regression neural network providing case-specific uncertainty estimates. This captures uncertainty that arises from the ill-posed nature of the inversion problem and instrumental noise.

Retrievals performed on simulations show that retrieved FWP values closely match the reference values across a wide dynamic range, from 10 $\mathrm{kg\,m^{-2}}$ down to about 10 or 40 $\mathrm{g\,m^{-2}}$, depending on the criteria used. The associated mass-weighted mean altitude follows the reference values with an RMSE of 1 km for altitudes 2–12 km, for cases where $\mathrm{FWP} \geq 0.1\,\mathrm{kg\,m^{-2}}$. The RMSE increases up to 2 km outside of this altitude range. Particle size estimates show systematic differences compared to reference values, except for sizes of 400 µm, with RMSE values increasing from 50 µm to 200 µm. Comparisons with other datasets provide evidence that these results extend to retrievals from real observations; for example, local means show a spatial distribution of FWP and zonal means that match those of existing radar/lidar-based retrieval products. For intense convective cores over land and ice/snow-covered surfaces, performance remains limited.

Direct validation against accurate satellite cloud radar retrievals is not possible due to insufficient co-located data. Instead, we compare to co-located IR-based retrievals trained on cloud radar data. The differences between our retrievals and the IR-based retrieval reproduce the reported differences between the IR-based retrieval and its radar-based training data. These results indicate that, compared with previous passive satellite retrievals, our FWP retrievals are closer in accuracy to cloud radar based retrievals.

The dataset complements cloud radar observations by providing a significantly broader swath (800 km compared to about 1 km). There is also potential to create a climate-relevant dataset, as the retrievals are directly applicable to the EPS-Sterna constellation, continuing the observations up to the year 2042.

1 Introduction

Atmospheric ice affects climate and weather patterns in multiple different ways. Ice hydrometeors are involved in 50% of precipitation events with $> 1\,\mathrm{mm}$ precipitation (Field and Heymsfield, 2015), release latent heat during formation that contributes to convective core growth (Bony et al., 2015), and influence the Earth's energy balance through various climate feedbacks (Intergovernmental Panel on Climate Change (IPCC), 2023, p. 95). Reliable and accurate global measurements of atmospheric ice are essential for detecting, verifying, and tracking these processes.

For more than 30 years, frequencies above $300\,\mathrm{GHz}$ have been identified as being of high interest for improving measurements of ice hydrometeor properties, particularly their mass (Gasiewski, 1992; Evans and Stephens, 1995). During these three decades, insights have been gained from simulations (e.g. Evans et al., 2002; Miao et al., 2003; Ekelund et al., 2020) and air-borne instruments (Wang et al., 1998; Evans et al., 2005; Fox, 2020; Pfreundschuh et al., 2022). Observations from space have been made (Wu et al., 2008; Eriksson et al., 2014), but limited to limb sounding, a measurement geometry less suited for ice hydrometeor retrievals. This changed in 2024 with the launch of the Arctic Weather Satellite (AWS; Eriksson et al. 2025). For the first time, regular downward-looking data with global coverage became available. Here, we present the first dataset of ice hydrometeor properties based on AWS.

Satellite-based retrievals of cloud ice properties have been limited to measurements at each end of the electromagnetic spectrum. Optical and infrared passive sensors observe ice clouds at wavelengths up to about $\lambda = 15\,\mu\mathrm{m}$, and on the long wavelength side, operational microwave radiometers have been limited to frequencies below $200\,\mathrm{GHz}$ ($\lambda = 1.5\,\mathrm{mm}$). It is noteworthy that the frequency/wavelength ratio between these two limits is 100. This ratio is even higher for active measurements, about 3000. Cloud lidars and radars to date operate at 355 - 1064 nm and $94\,\mathrm{GHz}$ (about 3mm), respectively. Being restricted to relatively short and long wavelengths results in challenges for retrievals. Short-wave observations are characterised by the strong impact of the more numerous small particles, and the information provided by these measurements is often limited to the cloud top layer (e.g. Eliasson et al., 2011). On the other hand, microwave observations, both active and passive, can sound the interiors of cloud systems, but the measured signal is dominated by the locally largest particles (Buehler et al., 2012, Fig. 3a).

These differences in sensitivity, in terms of particle size and cloud penetration, have led to poor agreement between satellite-based estimates of ice mass (Waliser et al., 2009). Retrievals combining satellite lidar and radar data are considered the most accurate, due to the high vertical resolution and sensitivity to both small and large ice hydrometeors. Still, the presently leading examples, DARDAR (Cazenave et al., 2019) and 2C-ICE (Deng et al., 2015), differ by 20 % even for global mean ice column mass (Eriksson et al., 2026). A main limitation of these datasets based on active observations is their limited spatial coverage (Eliasson et al., 2011), which underscores the need for ice mass retrievals based on passive observations.

Ice mass datasets based on passive data have, in general, given lower estimates compared to those based on active observations (Eliasson et al., 2013; Duncan and Eriksson, 2018). This can largely be understood by the fact that particle sizes and altitudes not sensed by the passive instruments are not included in the estimates.

Some newer passive retrievals compensate for this by applying machine learning, using e.g. 2C-ICE collocations as training data (Holl et al., 2014; Amell et al., 2024; Yang et al., 2026). Such approaches can mitigate biases with respect to the training data (Pfreundschuh et al., 2025). However, biases in the training data are inherited, and the methods provide no new physical insights. Such machine-learning approaches operate as black boxes, mapping sensor data to estimated quantity without transparent assumptions on microphysics and particle models, making new insights about such processes difficult to extract. Moreover, the retrieval precision remains relatively poor due to the physical limitations of the passive observations such as low sensitivity to certain particle size ranges and altitude depths.

Sub-millimetre measurements have the potential to fill the sensitivity gap between microwave and infrared wavelengths (Wu et al., 2024). The sub-millimetre range is a continuation of the microwave domain starting at 300 GHz ($\lambda = 1\,\mathrm{mm}$). The range's upper limit is often set to 3 THz ($\lambda = 0.1\,\mathrm{mm}$), but high absorption due to water vapour strongly limits the altitude coverage from about 1 THz ($\lambda = 0.33\,\mathrm{mm}$). Key features of sub-millimetre measurements as input for satellite-based ice mass retrievals are that they offer sensitivity across a broad range of ice masses (Evans et al., 1998; Jimenez et al., 2007) at the same time as providing broad altitude coverage (Evans et al., 2012; May and Eriksson, 2025).

To fully exploit the opportunities offered by the sub-millimetre range, satellite-based downward-looking observations are required. Several such satellite missions have been formulated (e.g. Miao et al., 2002; Buehler et al., 2012). Among the successful proposals, the most ambitious mission is the Ice Cloud Imager (ICI; Eriksson et al. 2020), with three such sensors to be launched as part of the second generation of the EUMETSAT Polar System (EPS-SG; Mattioli et al. 2019). The first launch involving ICI is planned for 2027. About one year later, the two small PolSIR satellites, each carrying a 325 and 680 GHz radiometer, are expected to be launched. The scientific objectives of PolSIR are related to diurnal variations of tropical ice clouds (Bennartz and Wu, 2025). An even smaller satellite, the IceCube technology demonstration mission, performed measurements around 880 GHz for 15 months (2017-18; Gong et al. 2021).

AWS was not designed with ice mass retrievals in mind; its main justification is to provide microwave data for numerical weather prediction (NWP) in a more timely and cost-effective manner. Nevertheless, the design of the AWS radiometer came to include a receiver with four channels around 325 GHz, to improve the treatment of ice clouds (Kaur et al., 2021). Consequently, it became the first operational mission to provide sub-millimetre data (Eriksson et al., 2025). These observations will be continued by the EPS-Sterna constellation, consisting of copies of AWS (Rivoire et al., 2024). The first batch of satellites in this constellation is planned to launch 2029, providing a continuous data record of both ICI and AWS sub-millimetre measurements that extend to 2045.

Accurately representing atmospheric ice in atmospheric models remains a major challenge; models have long shown a large spread in their estimates of cloud ice mass (Waliser et al., 2009). Although improvements are seen in newer generations (CMIP6), the intermodel spread remains high, and models remain biased low relative to observations (Lauer et al., 2023). This is a problem with direct consequences for the estimation of longwave cloud radiative effects (Bjordal et al., 2020). Global storm-resolving models (GSRMs) represent a step forward. Operating at a finer spatial resolution, these models explicitly resolve clouds and convective dynamics. Importantly, the output of GSRMs allows the derivation of total ice mass. This is the only quantity that can reasonably be compared across models and with observations, since partial amounts, such as "cloud ice",

are ambiguously defined. While GSRMs show improved agreement with observed total column ice, differences remain, both between models and with observations (Eriksson et al., 2026). Further progress requires multiple, independent observational datasets to verify atmospheric models from global to local scales.

We present the "Chalmers hydrometeor inversion product from the Arctic Weather Satellite" (CHIP-AWS): a level 2 (L2) product of ice hydrometeor mass retrievals from AWS. This first version of the retrieval product is designed to be comparable to the operational product planned by EUMETSAT for ICI (Eriksson et al., 2020), but uses an updated machine-learning algorithm following May et al. (2024). The main retrieval variable is the frozen water path (FWP) with unit $\mathrm{kg\,m^{-2}}$. The term FWP indicates that the aim is to estimate total ice mass, not just cloud ice (the term is further motivated in Eriksson et al. 2026). As a step towards providing profiles of frozen water content (as done in May and Eriksson, 2025), FWP is accompanied by an estimate of the mass-weighted mean altitude. Size information is given as the full column mass-weighted mean diameter.

Previous passive retrievals have underestimated the global average FWP compared to cloud profiling radar (CPR) datasets from CloudSat, such as DARDAR and 2C-ICE, by about 50%. Even between passive datasets there has been a large spread in global averages (Duncan and Eriksson, 2018; Eriksson et al., 2026). As will be motivated in the following sections, this dataset contributes improved accuracy to FWP retrievals and zonal averages comparable to CPR-based retrievals.

The AWS measurements are inverted into these quantities using a machine learning (ML) model trained to act as a non-linear predictor, taking antenna temperatures T_a as input and outputting estimates. A quantile regression neural network (QRNN; Pfreundschuh et al. 2018) is applied to provide case-specific retrieval uncertainties. Such a detailed error description is so far rare for machine learning-based datasets. Furthermore, to the best of our knowledge, operational machine learning models for cloud retrievals have exclusively been trained on existing retrievals, whereas our AWS retrievals use a ML-model trained on in-house simulated observations from radiative transfer simulations, driven by CloudSat radar reflectivities, making all microphysics assumptions explicit and possible to change with relative ease.

To perform sufficiently accurate simulations is a demanding task, but could not be avoided. As AWS had not yet launched, co-locating the new sub-millimetre observations directly with estimates from an existing dataset was not possible. After launch, co-locations with a satellite cloud radar could in principle be used (as done in Holl et al., 2014; Amell et al., 2024; Yang et al., 2026); however, no co-locations exists with AWS outside of the polar regions, giving insufficient global coverage. Instead a simulation database was built for training.

This approach offers two major advantages. First, it allows observations associated with poor retrieval performance to be compared against similar cases in the simulation database, where a coherent set of microphysics assumptions can be interrogated to gain new insights. Second, it accounts for variations arising from different particle habit and size distribution assumptions in the retrieval uncertainty estimates.

This first version of the dataset covers $\pm 60^\circ$ in latitude and off-nadir scan angles within 30°. These limitations are in place to prioritise good results for most areas before extending coverage. Retrievals are performed over all surfaces, though accuracy is lower over intense convection over land, and over land at higher latitudes with dry atmosphere and cold surfaces. The intention is to remove these constraints and limitations in future versions.

2 Source and reference data

This section introduces the instrument and input data used to produce the data product described in this article, as well as the reference data used for comparisons.

2.1 The Arctic Weather Satellite

AWS was launched into a sun-synchronous orbit in August 2024 and became fully operational at the beginning of 2025. The mean altitude of the orbit is about 590 km and the local time of the ascending node (LTAN) is 22:38. It carries, as its sole instrument, an across-track scanning radiometer. Here, a rotating parabolic mirror provides 145 so called field-of-views (fovs) covering roughly $\pm 54^{\circ}$ in scan angle range perpendicular to the satellite's flight direction. The radiometer has 19 channels over four frequency bands; AWS 11-18 (50 GHz), AWS21 (89 GHz), AWS 31-36 (183 GHz) and AWS 41-44 (325 GHz) corresponding to one feed-horn and receiver-chain for each band (Eriksson et al., 2025). The processed L1b files (EUMETSAT, 2024) give measured radiances in terms of antenna temperatures T_a with unit kelvin (K) for each channel, field-of-view, and scan.

In this work, channels AWS 21-44 are used, i.e. the 11 channels that include 89 GHz and above. The Earth-surface footprints for the 89 GHz, 183 GHz and 325 GHz receiver pairs have a full-width-at-half-maximum (FWHM) size of 20, 10, and 10 km, respectively, when the scanning mirror is pointing toward nadir (straight down).

In an effort to simplify the instrument, alignment optics were omitted and the four feed-horns are therefore slightly off the optical axis of the across-track scanning mirror. This results in different Earth-surface footprint locations for channels belonging to different receivers (see Fig. 5 of Eriksson et al., 2025 for more details). This has implications for using the measurements. To approximate a common propagation path between channel values, the values for AWS 21 and AWS 41-44 are re-interpolated onto the footprint locations of the grid defined by the 183 GHz channel footprints.

The mirror angles, the rotation angles of the parabolic mirror from nadir, for the different measurements are not provided in the L1b files. Instead, they provide satellite zenith angles, i.e. the angle from zenith at Earth-surface footprint locations to the satellite. The mirror angle can be approximated by geometrically determining the zenith angle in the satellite's reference frame at the expected altitude. These approximated mirror angles align with the simulated training data produced for this work (Sect. 4.1).

Systematic instrument biases in measured T_a values are corrected for. These bias corrections are informed by observation-minus-background (O-B) analysis of AWS T_a values performed by ECMWF (David Duncan, ECMWF, private communication). A live plot of O-B values for AWS is provided at https://charts.ecmwf.int/catalogue/packages/obstat/ (last access 2026-01-29). These corrections are mainly constant offsets, with two exceptions: the 183 GHz channels all have biases that change linearly across the scan's fovs, and channel AWS35 (181.5 GHz) has an additional bias that varies with latitude. Our corrections also take these variations into account. See the supplemental material for exactly how these bias corrections are applied.

For simulating the instrument, sensor characteristics are needed. In this work, measured instrument noise, spectral response functions, and footprint FWHM sizes are used as reported in Eriksson et al. (2025, Sect. 4.1 and Table 4).

2.2 ERA5, static data, and models

ERA5 hourly data on pressure levels and single levels (Hersbach et al., 2023a, b) are used to define the background atmospheric state in simulations. The variables include single-level data such as skin temperature, 2-metre temperature, 10-metre U and V wind components, and surface pressure, as well as pressure-level data such as temperature, geopotential, specific humidity, ozone mass mixing ratio, and specific cloud liquid water content. All 37 pressure levels from 1000 to 1 hPa are used and interpolated to the simulation grid (Sect. 4.1).

Furthermore, simulation surface properties are derived from a digital elevation map (GTOPO30; Earth Resources Observation and Science Center 2018) and a surface type classification (Copernicus land cover 100m; Buchhorn et al. 2020). The land cover classifications are further enhanced with dynamic effects by using ERA5 single-level variables: sea ice concentration and snow depth.

Additionally, scattering properties, emissivity models, and gas absorption models are used in the simulations. These are listed in Table 2. For more details and references, refer to May et al. (2024).

2.3 CloudSat reflectivities

CloudSat (Stephens et al., 2002) was operational between 2006 and 2023 and carried the cloud profiling radar (CPR) as its main instrument. The satellite's track, measurement timestamps, and radar reflectivities are utilised to drive the simulations described later in Sect. 4.1. The radar reflectivities are used to infer the frozen water content and rain water content that set the scene to be simulated, following the method described in May et al. (2024, Sect. 3.2).

The complete 2015 record was used. That year was chosen for practical reasons. Although 2015 coincided with a strong El Niño, the database covers a full annual cycle at all latitudes of the retrieval domain, and the retrieval model is given no information on time or location. El Niño mainly affects cloud occurrence and distribution, whereas the retrievals presented in this work use the relationship between individual cloud scenes and their radiative signatures. The 2015 record captures this relationship across a wide range of conditions. However, the changes in cloud distribution associated with El Niño may, to some extent, influence the prior of the retrieval.

2.4 Comparison datasets

Retrievals are validated through two approaches. First, we compare retrievals performed on simulated observations from a held-out test subset against the true CloudSat-derived values used to drive the radiative transfer simulations. Second, we compare retrievals from actual AWS observations with estimates from established datasets described below.

We include two passive datasets that retrieve ice water path from visible and infrared wavelengths: The Moderate Resolution Imaging Spectroradiometer (MODIS; Platnick et al. 2003) level 3 cloud properties product (Platnick and M. King, 2017b, a)

and CLARA-A3 (Karlsson et al., 2023a). Both datasets provide long-term records of cloud ice water path with associated uncertainties, though are limited to daytime observations. CLARA-A3 shows higher values over land and lower values over oceans compared to MODIS. However, globally the average difference is insignificant. See Karlsson et al. (2023b) for details on CLARA-A3's performance.

Both MODIS and CLARA use the bispectral solar reflectance method (Nakajima and King, 1990) to estimate cloud optical thickness and effective particle radius from visible and infrared wavelengths. Ice water path is derived from these retrieved quantities. Because ice water path is estimated from optical thickness and effective particle radius, these retrievals are sensitive primarily to the upper layers of deep clouds and miss the full column. The MODIS and CLARA datasets provide useful long-term comparisons of distributions and illustrate the bias from incomplete ice detection of deeper clouds. We compare our FWP retrievals with MODIS using local and zonal means, and with CLARA using zonal means and occurrence distributions.

We also include the Chalmers Cloud Ice Climatology (CCIC; Amell et al. 2024), which provides global FWP estimates at high temporal resolution across 60° S to 60° N every half hour. The method processes combined geostationary infrared images (Janowiak et al., 2001) through a neural network model trained on 3.5 years of the CloudSat-CALIPSO-derived 2C-ICE (Deng et al., 2015), a cloud properties retrieval dataset. CCIC produces FWP retrievals with associated uncertainty estimates that match 2C-ICE FWP in zonal-means values. The estimates are less precise than radar-based retrievals, underestimating values above $1\,\mathrm{kg\,m^{-2}}$ and overestimating values below, attributable to CCIC only using $11\,\mu\mathrm{m}$ wavelength data as input. Nevertheless, CCIC manages to retrieve cases with FWP values up to $10\,\mathrm{kg\,m^{-2}}$. See Amell et al. (2024) and Pfreundschuh et al. (2025) for further validation details. We include CCIC data as a comparison product for two reasons: it provides an independent passive (IR-based) FWP estimate via an ML-approach that achieves a zonal mean comparable to radar/lidar-based retrievals, and it is the only FWP dataset with sufficient temporal-spatial coverage to provide co-locations with AWS.

In addition, the DARDAR-CLOUD v3 (Cazenave et al., 2019) data product is used, providing ice cloud estimates of microphysical properties. This product is derived by combining measurements from CloudSat's CPR with lidar measurements from CALIPSO, covering the whole spectrum of particle sizes. We use DARDAR retrievals as a strong benchmark for FWP, and mass-weighted altitude and particle sizes in zonal means comparisons. DARDAR is chosen over 2C-ICE to provide another cloud radar comparison, since CCIC uses the latter for training. Although CloudSat CPR reflectivities serve as input for both DARDAR (and 2C-ICE) and our simulations, the inversion from reflectivities to frozen water content in the simulations presented in this work is independent of the method employed by DARDAR. We argue that this independence makes DARDAR a valid comparison product.

3 The data product

3.1 Description

CHIP-AWS is a dataset of atmospheric ice-mass estimates that have been retrieved from calibrated antenna temperature (T_a) values from AWS's across-track scanning radiometer. AWS data from January 2025 and onwards are continuously processed and available at http://clouds-and-precip.group/datasets/chip-aws. An archival copy of full 2025 data can be accessed under

Variable	Dimensions	Description
Frozen water path ($\mathrm{kg\,m^{-2}}$)	(scan, fov)	Mass of ice hydrometeors in a vertical column through the atmosphere.
Z_m (m)	(scan, fov)	Mass-weighted mean altitude of ice hydrometeors inside the column.
D_m (m)	(scan, fov)	Mass-weighted mean volume-equivalent diameter of ice hydrometeors inside the column.

Auxiliary Variable	Dimensions	Description
Surface type fractions	(scan, fov, surface_type)	Fraction of footprint covered by: Ocean, Sea Ice, Land, Water, Snow and Glacier.
T_a (K)	(scan, fov, channel)	Reinterpolated and bias-corrected antenna temperatures used for the retrieval.
Remap distance (m)	(scan, fov)	Distance between AWS3X and the nearest AWS4X footprint in the reinterpolation window. This can be used to filter for cases that required little reinterpolation.
CCIC FWP ($\mathrm{kg\,m^{-2}}$)	(scan, fov)	Co-located FWP estimates from the Chalmers Cloud Ice Climatology (CCIC). An independent retrieval method based on geostationary IR.
Incidence angle (°)	(fov)	Mean of "Satellite Zenith Angle" values reported by source L1b file. Unreasonable values are removed before averaging (see Sect. 3.3).
Altitude (m)	scalar	Mean of "Satellite Altitude" values reported by source L1b file. Unreasonable values are removed before averaging (see Sect. 3.3).

Table 1. Estimated variables and auxiliary variables in CHIP-AWS. Estimates for the main variables are given as a “mean” (the mean of the retrieved CDF), “most probable” (value at peak PDF) and the 0.02, 0.16, 0.5, 0.84, and 0.98 quantiles of the CDF.

data DOI https://doi.org/10.71870/v9dx-rm43 (McEvoy, May, and Eriksson, 2026). The retrievals are performed footprint by footprint and constitute a quasi-global (60° S to 60° N) level 2 processing of level 1b AWS data.

Table 1 shows the variables included in this dataset. There are three main variables: frozen water path (FWP) with unit $\mathrm{kg\,m^{-2}}$, Z_m with unit m, and D_m with unit m (see Sect. 3.2 for a definition of these quantities). These are given in the along-track "scan" dimension and the across-track "field-of-view" (fov) dimension with 88 elements corresponding to incidence angles $< 37^\circ$, resulting in a swath width of about $800\,\mathrm{km}$.

For each retrieval, the method estimates quantiles for the three quantities at fixed quantile levels that characterise the posterior cumulative distribution function (CDF). The method derives and stores the mean of the retrieved CDF, the "most probable value" (peak of the PDF), and the 0.02, 0.16, 0.5, 0.84, and 0.98 quantiles. This quantile-based approach captures the uncertainty, addressing the ill-posed nature of the inversion problem, where multiple distinct scenarios can produce similar observed signals (see Sect. 4.2 for details and definitions). Throughout this text, unless specified otherwise, our retrieval "estimates" refers to the mean of the retrieved CDF.

The dataset includes auxiliary variables for each observation. These consist of the ratios of different land cover types that the observation footprint covers (enabling filtering by surface type), and the bias-corrected and re-interpolated antenna temperatures used as input to the retrieval method. The distance between footprints used for re-interpolation is also provided, allowing filtering or inspection of interpolation distances.

3.2 Quantity definitions

Frozen water content (FWC) is the mass of frozen water per unit volume ($\mathrm{kg\,m^{-3}}$). It can be expressed as

$$\mathrm{FWC} = \int_0^\infty m(d_\mathrm{veq}) n(d_\mathrm{veq}, z)\,\mathrm{d}d_\mathrm{veq}\,, \tag{1}$$

where n is the particle size distribution (PSD), m is the particle mass and d_veq is the volume-equivalent particle diameter ($d_\mathrm{veq} = \sqrt[3]{6m/\pi\rho}$), with m and ρ being the particle mass and the density of (solid) ice, respectively.

The main retrieval quantities are defined as follows. FWP is the vertical integral (from surface altitude z_0) over FWC,

$$\mathrm{FWP} = \int_{z_0}^\infty \mathrm{FWC}\,\mathrm{d}z\,. \tag{2}$$

The mass-weighted mean altitude Z_m is defined as

$$\mathrm{Z_m} = \frac{\int_{z_0}^\infty z\mathrm{FWC}\,\mathrm{d}z}{\mathrm{FWP}}\,. \tag{3}$$

Finally, the mass-weighted mean particle diameter D_m is defined as

$$\mathrm{D_m} = \frac{\overbrace{\int_0^\infty d_\mathrm{veq}^4 \int_{z_0}^\infty n(d_\mathrm{veq}, z)\,\mathrm{d}z\,\mathrm{d}d_\mathrm{veq}}^{\text{4th moment}}}{\underbrace{\int_0^\infty d_\mathrm{veq}^3 \int_{z_0}^\infty n(d_\mathrm{veq}, z)\,\mathrm{d}z\,\mathrm{d}d_\mathrm{veq}}_{\text{3rd moment}}}\,. \tag{4}$$

This is consistent with Delanoë et al. (2014), Eq. (3), with the exception that their size parameter is defined with respect to the melted equivalent diameter. Equation A9 in Amell et al. (2022) shows that this expression is the column-integrated FWC-weighted particle size. For a more rigorous definition of these quantities that consider the radial sensitivity of measurement footprints, refer to Eq. (1–3) in Eriksson et al. (2020).

3.3 Spatio-temporal coverage and resolution

AWS measures continuously along its sun-synchronous orbit. In this dataset, measurements are provided in the instrument's native scan and field-of-view dimensions. This first version of the dataset is restricted to latitudes between 60° S and 60° N and the number of field-of-views has been reduced from 145 to 88 elements to reduce incidence angles. These restrictions are put in place to reduce the complexity of this initial version, with concerns for simulation capabilities over polar regions regarding surfaces and extreme incidence angles in mind. Future work aims to extend the retrievals to broader swaths and fully global coverage.

The combination of this swath width, the sun-synchronous orbit, and data processing results in median revisit times (per pass direction) of approximately one day globally. While the median is one day across latitudes, the 75th percentile increases from five days at mid-latitudes to approximately seven days in the tropics. For further details on revisit time, see Appendix B.

This dataset includes estimates for all of 2025 and onwards as new retrievals are regularly processed. However, due to AWS commissioning tests and data processor updates, there are more frequent data gaps at the beginning of the year. From 2025-03-21 and onwards, gaps are less frequent.

The instrument performs a full scan every $1.19\,\mathrm{s}$, resulting in an along-track sampling distance of $8\,\mathrm{km}$. The instrument's scanning motion leads to a varying sampling distance across-track, ranging from 8 to $12\,\mathrm{km}$, for scan angles limited to 30° from nadir. The footprint size depends on the input channels. Out of the 11 input channels used to produce this dataset 10 have a nadir footprint FWHM size of $10\,\mathrm{km}$, while only AWS21 ($89\,\mathrm{GHz}$) has a nadir footprint size of $20\,\mathrm{km}$. Due to having 10 out of 11 channels with the smaller footprint size, we argue that the nominal footprint of the retrieval method is closer to $10\,\mathrm{km}$ at nadir.

The major d_a (across-track) and minor d_b (along-track) diameters of the ellipse approximating the footprint FWHM size depend on the incidence angle θ (the angle between local zenith and the satellite) as follows:

$$d_b(\theta) \approx \left(\sqrt{(R+h)^2 - R^2\sin^2\theta} - R\cos\theta\right)\frac{d_n}{h}, \tag{5}$$

$$d_a(\theta) \approx \frac{d_b(\theta)}{\cos\theta}, \tag{6}$$

where R is Earth's radius, h is the satellite's altitude, and d_n is the footprint FWHM size at nadir. With these expressions, the footprint size can be calculated for each observation using incidence angles and satellite altitudes. The retrievals include averaged incidence angles for each field-of-view and averaged satellite altitudes, from each source L1b file. Unreasonable incidence angles (outside of range 0–180°) and altitudes (outside of range 400–$800\,\mathrm{km}$) as well as values associated with a non-zero L1b quality flag are excluded from averaging. For the extreme scan-angles in this dataset $10\,\mathrm{km}$ nadir FWHM size is scaled to $14\,\mathrm{km}$ across-track and $11.7\,\mathrm{km}$ along-track.

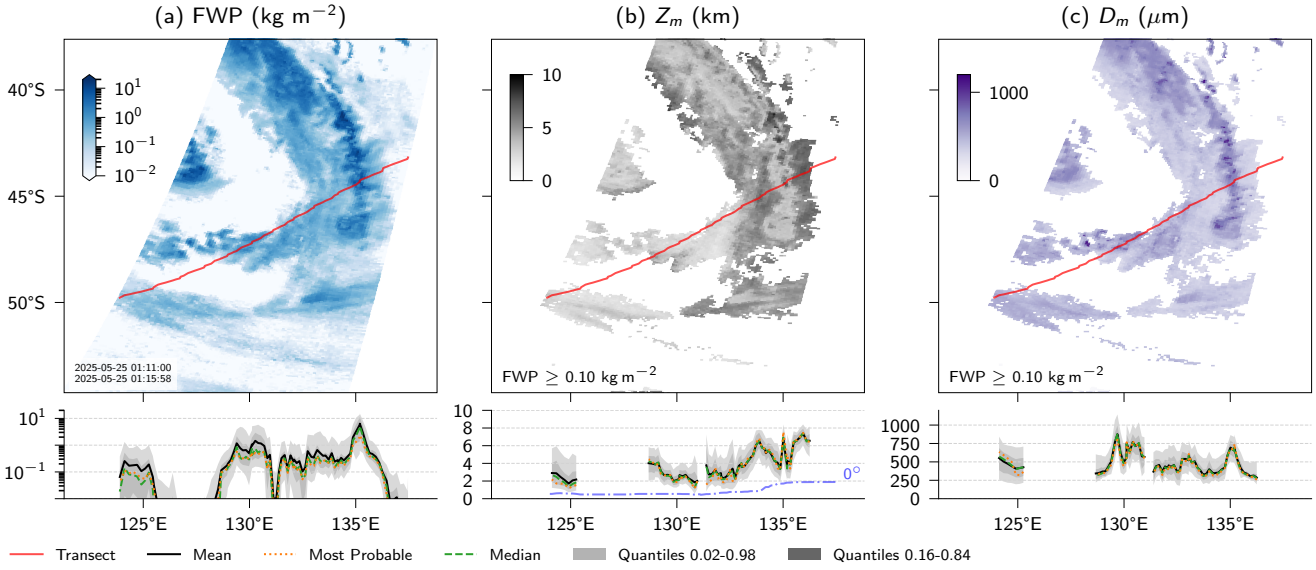


Figure 1. An example of CHIP-AWS data: a weather system south of Australia. Top row shows mean values derived from the retrieved CDF for the three ice-mass-related variables: FWP, Z_m, and D_m. Bottom row shows all available estimates sampled along the transect line and projected onto the longitude axis: the "mean" (the average of the retrieved CDF), the "most probable" (corresponding to the maximum of the retrieved PDF), and the quantiles. For Z_m, transect values additionally include a 0° isotherm from ERA5.

Despite the fact that AWS observes the atmosphere from a slanted angle off-nadir, the dataset values for FWP, Z_m and D_m are estimates of vertical columns from the Earth's surface. The model behind the retrieval is trained to scale estimates to account for the extra integration path.

3.4 Example scene

We demonstrate the available variables and estimates using example scenes from the dataset. Figure 1 shows a weather system south of Australia with varying intensity of clouds across the scene. The retrievals from this scene reveal a wide range of values for all three variables: clear-sky conditions, areas with little ice, thicker clouds, and intense centres. The mass-weighted mean properties Z_m and D_m likewise show considerable variation.

A transect is chosen to intersect regions of varying FWP values across both the field-of-view and scan dimensions. For FWP (Fig. 1a) transect values close to 125° E, uncertainty is high (wide quantile span), while the retrievals are relatively more certain for higher values near 135° E. This demonstrates how the dataset conveys uncertainty and that estimated values are more certain when there is more ice to sense.

For mean mass-weighted altitude Z_m and particle size D_m (Fig. 1b-c), in regions with higher FWP, we observe a low-altitude segment around 125° E and a high-altitude segment near 135° E. Notably, regions with different particle sizes can exhibit uniform FWP estimates (such as 50° S, 135° E), indicating that particle sizes can vary independently of FWP.

Note that estimates for Z_m and D_m are masked when mean FWP estimates fall below the threshold of $0.1\,\mathrm{kg\,m^{-2}}$. Although the dataset provides values and quantiles for all variables in all cases, the high uncertainty for the mass-weighted properties at low FWP renders the mean estimate (mean of the retrieved CDF) uninformative. The threshold is not strict, but our choice is further motivated in Sect. 5.2.2.

The example scene illustrates dataset variables and the relationships between them. It is evident that both Z_m and D_m exhibit higher certainty only when FWP values are significant, emphasizing the importance of also considering FWP when interpreting these estimates.

Figure 2 shows a tropical scene and demonstrates how the retrieved quantiles can be applied to provide classification probabilities. This example uses tropical ice cloud FWP classifications introduced by Sokol and Hartmann (2020): convective cores ($\mathrm{FWP} \geq 1\,\mathrm{kg\,m^{-2}}$), thin cirrus ($10^{-3} \leq \mathrm{FWP} \leq 10^{-2}\,\mathrm{kg\,m^{-2}}$), and anvil cirrus for values in-between. We add an additional classification for clear-sky ($\mathrm{FWP} \leq 10^{-3}\,\mathrm{kg\,m^{-2}}$). For each point, the quantile values and corresponding quantile levels are used to sample the CDF at the relevant threshold, representing the probability that FWP falls below it. Class probabilities are obtained by taking the difference between these threshold probabilities.

In this example, convective cores, anvil cirrus and clear-sky cases can be classified with substantial probabilities, at or close to one. The thin-cirrus classification gives the probability consistently below 30%, likely due to poorer instrument sensitivity in this FWP range (Sect. 5.2.2).

4 Retrieval method

The retrieval method is based on the preparatory work for the Ice Cloud Imager (ICI) to be carried by Metop-SG-B described in May et al. (2024). In short, detailed radiative transfer simulations produce a database of simulated instrument antenna temperature (T_a) values and corresponding scene parameters (FWP, Z_m, D_m). The database is then used to train a neural network. Here, QRNNs give a model that produces quantiles and thus CDFs of the physical parameters based on the T_a input. To get final estimates, real T_a observations from AWS are re-interpolated and bias-corrected (Sect. 2.1), before being fed into the trained QRNN model. More detail on the simulation, training, and inference steps, as well as key differences from May et al. (2024), follows.

4.1 Simulation database

Radiative transfer simulations with ice-particles were performed with ARTS version 2.6 (Buehler et al., 2025). The ARTS database for single-scattering properties of ice hydrometeors (Eriksson et al., 2018) was used, which includes data into the sub-millimetre wavelength range.

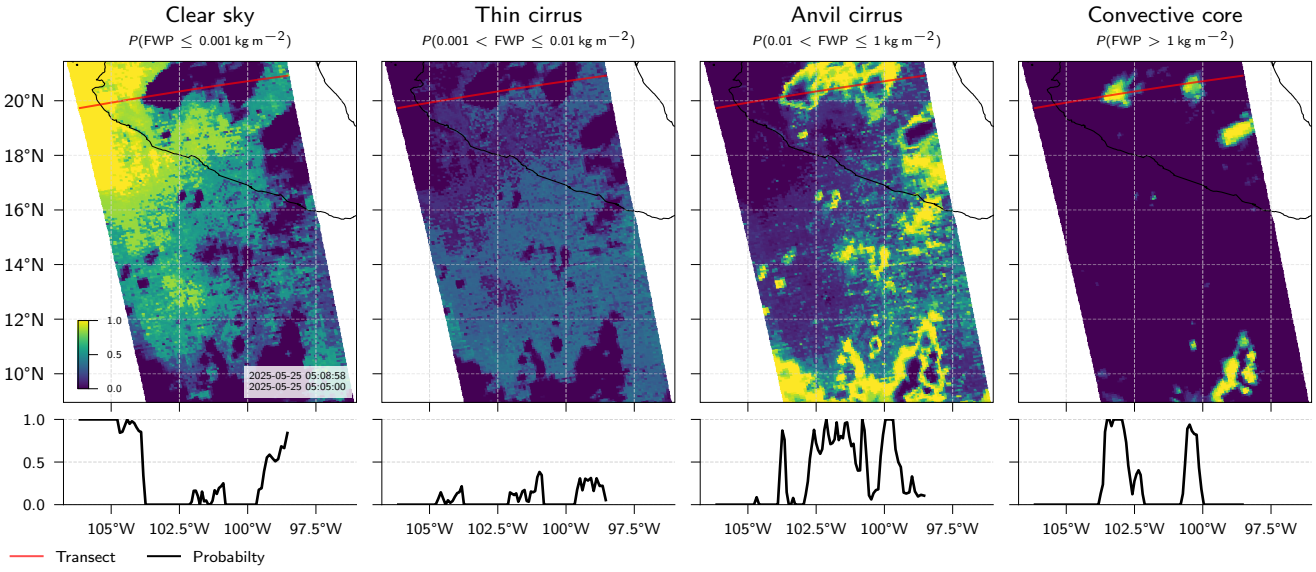


Figure 2. A scene from the eastern tropical Pacific, off the coast of southern Mexico. Classification probabilities are calculated using provided per-retrieval quantiles. The FWP ranges for convective core, anvil cirrus and thin cirrus are taken from Sokol and Hartmann (2020). A transect intersects regions with significant probability across most classes; probability values extracted from the transect are projected onto longitude coordinates and shown in the bottom row.

For each simulation, an ice particle model, defined as a pairing of an ice particle habit and a particle size distribution (PSD) model, is chosen. Table 2 in May et al. (2024) shows the set of six particle models used for the simulations in that work. In this work, simulations use the same set of particle models, however, with particle model "AA3" replaced. "AA3" (habit: Large block aggregate; PSD model: Delanoë et al. 2014) is replaced with a new particle model consisting of habit "IconHail" from the same scattering database and an exponential PSD model (Marshall and Palmer, 1948); $n(d_{\text{veq}}) = N_0 \exp(-\Lambda d_{\text{veq}})$, with $N_0 = 2 \times 10^7$ and the slope-parameter Λ left as a free parameter that is set to achieve the simulation scene's FWC value. This change of particle model was motivated by early AWS observations revealing discrepancies in areas of deep convection. We leave this analysis and further investigations on what the AWS data reveal about particle microphysics to a forthcoming study, keeping this work focused on the data product itself.

The driving input to the simulations are radar backscatter data from CloudSat's cloud profiling radar (CPR). For an input CloudSat segment, a 2D grid is set up with the along-track trajectory as one dimension (defined by the CloudSat segment's observation coordinates at native resolution) and altitude being the other. The altitude grid comprises 61 fixed pressure levels between $1100\,\text{hPa}$ and $50\,\text{hPa}$, and 39 levels between 45 and $1\,\text{hPa}$. CloudSat radar reflectivities are re-interpolated to these pressure levels.

The segment's latitude-longitude trajectory and timestamps are used to load complementary ERA5 data (Sect. 2.2) setting background properties such as humidity, surface skin temperature, and liquid water content (incl. super-cooled). With the grid

set, one of six particle models is chosen (weighted according to May et al. 2024), and the frozen water content and rain water content are estimated from the radar backscatter given the atmospheric state from ERA5, populating the scene's 2D grid with hydrometeor information.

This radar-retrieval method is referred to as ARTS onion peeling and is described in Sect. 2.1.2 of Eriksson et al. (2026) and Sect. 3.2 of May et al. (2024). However, unlike May et al. (2024), the scene here is kept as 2D, and the Barker method used there is not applied.

The scene is further refined by adjusting surface emissivity properties according to a land-cover dataset that incorporates dynamic ERA5 variables for sea-ice concentration and snow depth. TELSEM and TESSEM are used for land and ocean emissivity models, while ice and snow are modelled as a flat surface with varying reflectivities. All simulation inputs are listed in Table 2.

Basic quality filtering is applied, removing unphysical negative values. No attempt was made to adjust the ERA5 humidity field using radar data, even though such adjustment could address physical inconsistencies (Rydberg et al., 2007). Another limitation is that the melting layer is not included in simulations, as there currently is a lack of scattering data for melting particles appropriate for passive MW and sub-millimetre wavelengths.

Deriving FWC from CloudSat's CPR reflectivities keeps particle model assumptions consistent between scene population and passive AWS observation simulation. Alternative sources, such as CloudSat-derived products like DARDAR and 2C-ICE, or even ERA5, can provide direct FWC estimates, but have their own microphysics assumptions. Particle model assumptions add uncertainty. We capture this uncertainty by performing FWC inversions from CPR reflectivities and simulating observations using a randomly sampled particle model from a predefined set. The spread in simulated values informs the uncertainty estimates produced by the QRNN inversions.

On average, the FWP values from this radar inversion method are closer to DARDAR estimates than 2C-ICE in terms of zonal mean. Comparisons of this inversion method with DARDAR, 2C-ICE and other datasets, are available as zonal means and occurrence fractions in Eriksson et al. (2026, Fig. 2 and Fig. 4). The average impact of different particle models on the average retrieved FWP is presented in Table 5 of the same article.

With the scene populated, radiative transfer simulations of AWS observations can begin. The AWS instrument is simulated observing the full scene along the same track as the input CloudSat segment. Although the scene is 2D (along-track and altitude), a variation in the simulated across-track scan is achieved by the slant path effect from the varying scan angle. The instrument's frequency response is modelled using measured spectral response functions (SRFs) of the instrument channels (Eriksson et al., 2025).

A simulated segment, with a set particle model and mirror angle, results in pencil beam brightness temperatures every $3\,\mathrm{km}$ along-track. Groups of 15 consecutive pencil-beam values are weighted by a Gaussian distribution to model the instrument's footprint FWHM, resulting in a simulated antenna temperature T_a every $9\,\mathrm{km}$.

The full database is generated by performing simulations on the entire CloudSat radar dataset from 2015 multiple times with randomised properties such as particle model, scan angle, and segment selection. This process yields a database of 6,086,928 simulated AWS T_a values for each of the 11 channels, along with the corresponding scene parameters (FWP, Z_m, D_m).

Input	Purpose
CloudSat Radar Reflectivities	Set FWC and RWC. See Sect. 2.3.
ARTS single-scattering database	Simulate scattering with ice hydrometeors. See Sect. 2.2
ERA5 Variables	Set surface and atmospheric properties. See Sect. 2.2.
RTTOV v13	Gas absorption model.
TELSEM / TESSEM	Surface emissivity for land/ocean.
ARTS flat reflective surface	Model ice and snow through a flat surface with varying reflectivity.
Landcover	Selects surface emissivity model based on surface type.
DEM	Set surface elevation.
Sensor Characteristics	Instrument modelling. AWS spectral response function, footprint sizes and noise. See Sect. 2.1.

Table 2. Simulation inputs.

4.2 Inversion with QRNN

A QRNN machine learning model performs the inversions. We adopt the remote sensing nomenclature, where the state vector $\boldsymbol{x}$ is retrieved from the observation vector $\boldsymbol{y}$. The network is trained to perform this inversion using a dataset of paired observations and states $\{\boldsymbol{y}_i, \boldsymbol{x}_i\}_i^n$.

The inverse problem considered here is non-linear and ill-posed. As a result, an observation vector does not map to a single state vector, but rather to a region in state space. It is therefore more appropriate to take a probabilistic approach to the inverse problem and retrieve a description of the probability density function (PDF) of the state. A QRNN achieves this by estimating quantiles of the CDF of the state vector $\boldsymbol{x}$. It does this through the use of a quantile loss function (Pfreundschuh et al., 2018), defined as

$$\mathcal{L}_\tau(x_\tau, x) = \begin{cases} \tau|x - x_\tau|, & x_\tau < x \\ (1-\tau)|x_\tau - x|, & \text{otherwise.} \end{cases} \tag{7}$$

where $\tau \in [0, 1]$ denotes the quantile level. In our training, a set of 99 quantile levels with a bin size of 0.01 is used. By minimising the expectation of $\mathcal{L}_\tau(x_\tau, x)$, the model can estimate the τth quantile x_τ. By training the retrieval model to estimate multiple quantiles, a discrete approximation of the CDF is obtained per observation.

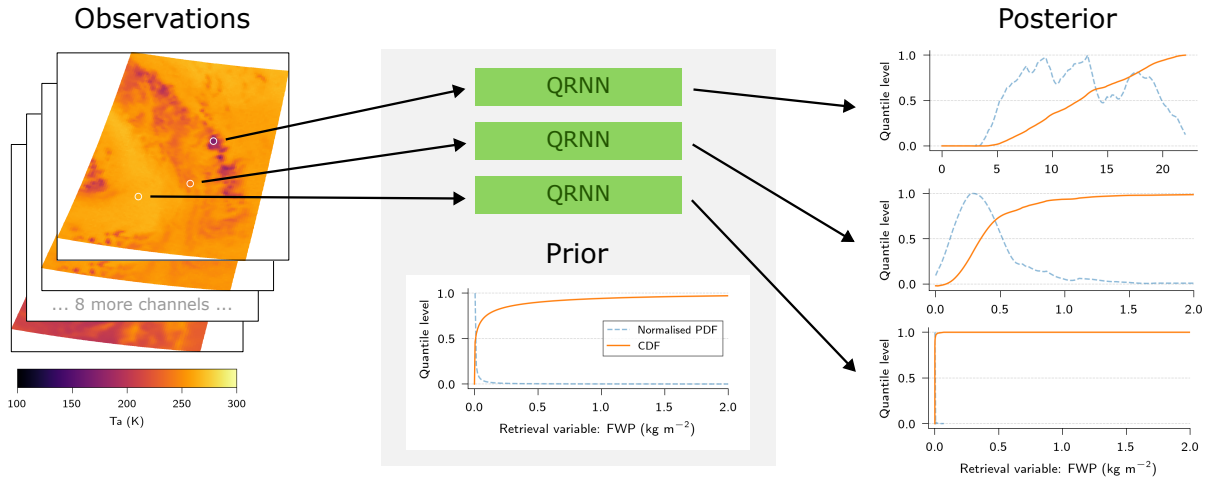


Figure 3. Illustration of QRNN updating quantiles for three example observations. Each observation comprises 11 T_a values. The model outputs quantile estimates interpretable as CDFs and PDFs, here PDFs are normalised so that maximum value equals 1. Both CDFs and PDFs are smoothed in this illustration.

The final model learns the distribution of its training data, which serves as the prior in a Bayesian framework. When given measurement inputs, this prior is updated with the new information and produces the posterior distribution. Figure 3 illustrates this on a real scene: measurements from an intense part of the scene shift the quantile values so that high FWP become more probable, whilst a clear-sky measurement shifts quantile values to much lower FWP. The most intense observation in this example predicts an almost equal probability for FWP between 5 and 20 $\mathrm{kg\,m^{-2}}$. This spread can reflect either the uncertainty from the multiple particle models in the simulation database or measurement channels being saturated for the FWP signal.

The retrieved quantiles can be interpreted as a CDF, from which two point estimates are obtained: the mean (expectation value) μ and the most-probable value $\hat{x}$. The mean μ is given by weighting values by the PDF $f(x)$, but it can also be expressed as integrating over the CDF (F):

$$\mu = \mathbf{E}[X] = \int_0^\infty x f(x)\,\mathrm{d}x = \int_0^\infty x\,\mathrm{d}F(x)\,. \tag{8}$$

The most-probable estimate $\hat{x}$ corresponds to the value at which the PDF is maximised,

$$\hat{x} = \arg\max_x f(x)\,. \tag{9}$$

Directly differentiating numerically estimated quantiles to obtain the PDF introduces unnecessary numerical error. Instead, for the mean, we construct a CDF from the quantiles and their levels, apply piecewise linear extrapolation to 0 and 100% probability, then apply trapezoidal integration to obtain the mean μ. Similarly, for the most-probable estimate, noise in the predicted CDF introduces significant artefacts when numerically differentiated. We therefore smooth the CDF before differentiation to robustly identify the peak.

Since the CDF represents the retrieval uncertainty arising from the ill-posed nature of the problem, i.e. the aleatoric uncertainty, the retrieved quantiles (or spread between them) constitute an observation-specific uncertainty measure. Accordingly, selected quantiles are provided alongside the single point retrieval estimates, as described in Sect. 3.1.

For CHIP-AWS, the QRNN input $\boldsymbol{y}$ is a vector consisting of a set of 11 antenna temperatures for channels in the 89, 183, and 325 GHz bands, and the mirror angle. The model output $\boldsymbol{x}$ corresponds to the scene parameters FWP, Z_m, and D_m. The list of inputs and outputs is presented in Table 3.

4.3 Training and inference

As described in Sect. 4.1, each simulation consists of a pairing of scene parameters $\boldsymbol{x}$ and corresponding simulated measurements $\boldsymbol{y}$, which together form the database $\{\boldsymbol{y}_i, \boldsymbol{x}_i\}_i^n$. The database is divided into 80 % training, 10 % validation and 10 % testing subsets. Subset division is performed by random selection of CloudSat segments and not individual observations. The training and validation subsets are fed to the model during training, while the test subset is reserved for evaluation.

Since FWP spans orders of magnitude, a log-linear transformation is applied to FWP prior to training: values less than $1\,\mathrm{kg\,m^{-2}}$ are transformed into logarithmic space, whilst those above are kept in linear space. Values below $10^{-4}\,\mathrm{kg\,m^{-2}}$ are replaced by random values uniformly sampled between 10^{-6} and $10^{-4}\,\mathrm{kg\,m^{-2}}$ and subsequently transformed into logarithmic space. As a consequence, the dataset has no estimates of zero FWP.

A single model is trained to output 99 uniformly spaced quantile levels ($\tau \in [0.01, 0.99]$) of the CDF for each retrieved variable. The network consists of 12 fully-connected layers with 512 neurons each that are shared across all output variables, followed by two variable-specific fully-connected layers (512 neurons each) that output the 99 quantile estimates.

When training, for each AWS channel, a random noise sample is generated by sampling from a Gaussian distribution with zero mean and a standard deviation corresponding to NEΔT on ground (OG), which is given in Eriksson et al. (2025, Table 4). New noise samples are generated each time a training sample is seen by the neural network, acting as a form of data augmentation.

Once trained, the model can perform retrievals on real observations. During inference, a bias-corrected AWS observation for a single scan and field-of-view is fed into the network. In the simulated training data, all input channels shared the same Earth-surface footprint, i.e. have a common propagation path. For consistency, the real observation is re-interpolated onto the AWS3X footprint (Sect. 2.1). Since the distance between the AWS3X and the nearest AWS4X footprint can vary by a significant amount (0.6–6 km), this remapping distance is provided as an auxiliary variable for inspection and filtering (see Table 1).

Feeding the re-interpolated and bias-corrected T_a values into the trained QRNN returns an estimated CDF in terms of quantiles for a given set of quantile levels for each variable. From this CDF, the mean and the most probable estimate are derived. The produced dataset files include five of the 99 quantiles: 0.02, 0.16, 0.5, 0.84, and 0.98, chosen to line up with median, $\pm 1\sigma$, and $\pm 2\sigma$.

Input variable	Description
AWS21 T_a	T_a at 89 GHz
AWS31 T_a	T_a at 165.5 GHz
AWS32 T_a	T_a at 176.311 GHz
AWS33 T_a	T_a at 178.811 GHz
AWS34 T_a	T_a at 180.311 GHz
AWS35 T_a	T_a at 181.510 GHz
AWS36 T_a	T_a at 182.311 GHz
AWS41 T_a	T_a at 325.15$\pm$1.2 GHz
AWS42 T_a	T_a at 325.15$\pm$2.4 GHz
AWS43 T_a	T_a at 325.15$\pm$4.1 GHz
AWS44 T_a	T_a at 325.15$\pm$6.6 GHz
Mirror angle	See Sect. 2.1.

Output variable	Description
FWP quantiles	Quantiles x_τ of the CDF of FWP, $\tau \in [0.01, 0.99]$.
Z_m quantiles	Quantiles x_τ of the CDF of Z_m, $\tau \in [0.01, 0.99]$.
D_m quantiles	Quantiles x_τ of the CDF of D_m, $\tau \in [0.01, 0.99]$.

Table 3. Inputs and outputs of the retrieval model. The T_a values listed as input variables are re-interpolated onto the AWS3X footprint locations and bias-corrected, with the names corresponding to the channel ID.

5 Results

In this section, we first demonstrate that the underlying simulation database (DB) represents observed atmospheric states. We assess retrievals on a held-out test subset of simulations, demonstrating ideal synthetic retrieval performance. Finally, we show retrieval results from real AWS observations and compare against other datasets.

5.1 Simulation database

Basing the retrieval training on simulations requires those simulations to represent atmospheric conditions accurately and to model radiative transfer correctly. We therefore examine the distribution of simulated T_a values and compare with observations from AWS. We first consider oceanic cases, to focus on the accuracy of the radiative transfer simulations with the best understood surface interaction.

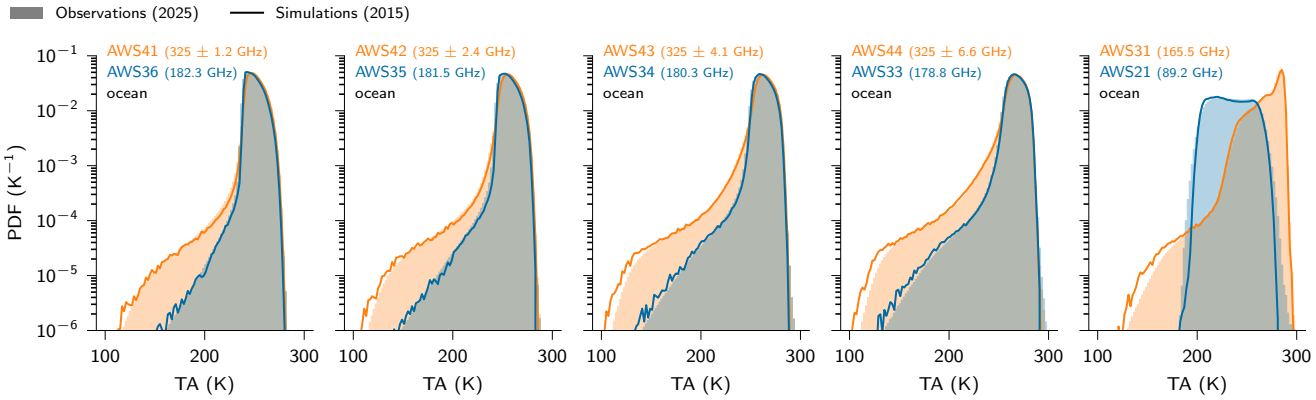


Figure 4. Distribution of simulated database T_a values (driven by CloudSat radar reflectivities from 2015) and distribution of actual observed T_a values from AWS 2025. Channels that have similar altitude of peak humidity sensitivity are paired. Both simulations and observations are filtered for ocean cases.

For these comparisons, recall that the simulations have the atmospheric state for hydrometeors driven by 2015 CloudSat radar reflectivities, whilst AWS observations are from 2025. Co-located simulations were not possible during this work due to CloudSat being decommissioned. Its successor, EarthCARE, was in commissioning phase at the time of writing and operates in an incompatible orbit. Despite this temporal mismatch with CloudSat, a sufficiently large sample size should ensure that the distribution of atmospheric states remains statistically representative, allowing for meaningful comparisons between the two.

5.1.1 Simulations and surface types

Figure 4 shows the T_a distributions from the simulation database and AWS observations over ocean for each retrieval input channel. The simulated and observed T_a distributions agree remarkably well, both in overall shape and in absolute values, including at the tails of the distributions. As a rule of thumb, T_a values below 250 K for the sub-millimetre channels are associated with clouds.

A more detailed comparison between simulations and observations can be seen in the interplay between channel responses. Figure 5 illustrates the observed and simulated joint probability densities of AWS33 (178.811 GHz) and AWS44 (325.15 ± 6.6 GHz) T_a values. These channels are paired due to having similar clear-sky Jacobians for humidity (Eriksson et al., 2025, their Fig. 12), i.e. can be seen to have a similar altitude sensitivity. This demonstrates that the simulated observations encompass the observed joint AWS33 and AWS44 T_a values with comparable density. This shows that the simulations not only replicate the distribution of individual channel values but also successfully simulate cases that affect multiple channels in a way that is consistent with real observations.

Over other surfaces, simulation performance is mixed. Over land, the performance is good, but channel AWS21 (89 GHz) simulations only extend down to about 200 K, while observations reach as low as 120 K. We attribute these low values to

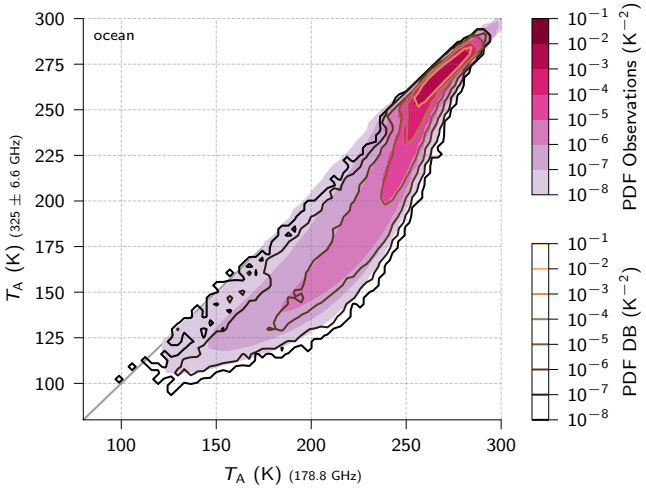


Figure 5. The 2D density plot of AWS33 (178.811 GHz) and AWS44 (325.15 ± 6.6 GHz) T_a values from observed and simulated cases. The shaded areas represent the density of observed cases (from all of 2025), while the contour lines overlay the density of simulated cases. Both simulations and observations are filtered for ocean cases.

intense tropical deep convective cores, cases that our simulations currently struggle to recreate. Here, larger hydrometeors such as snow, graupel, and hail dominate the scattering, and the modelling of their properties and particle size distributions likely remains inadequate for such intense cases. Scenes with cold surfaces and a dry atmosphere cause the most problems, often observed at higher latitudes and over sea-ice. To address these limitations, surface reflectivity for ice and snow as well as particle model assumptions for deep-convection will need adjustment informed by observational datasets. In the mean time, the surface type fractions provided for each estimate can be used to filter out these cases. For more details on the performance over these surfaces, see Appendix A.

5.2 Retrieval performance on simulations

Retrievals in this section are performed on the held-out test-subset of the simulation database to evaluate model retrieval performance in isolation.

5.2.1 Occurrence fractions

Figure 6a–c shows the occurrence fractions, i.e. binned value counts divided by total sample count, for FWP, Z_m, and D_m values retrieved from simulated T_a values. These are compared to the corresponding true database distribution (panels d–f show occurrence fractions from real observations and are addressed in Sect. 5.3).

The retrieved occurrence of FWP estimate values match the database distribution for values down to about $40\,\mathrm{g\,m^{-2}}$, after which retrievals start to overestimate the frequency of lower FWP values, indicating some loss of sensitivity in the retrievals.

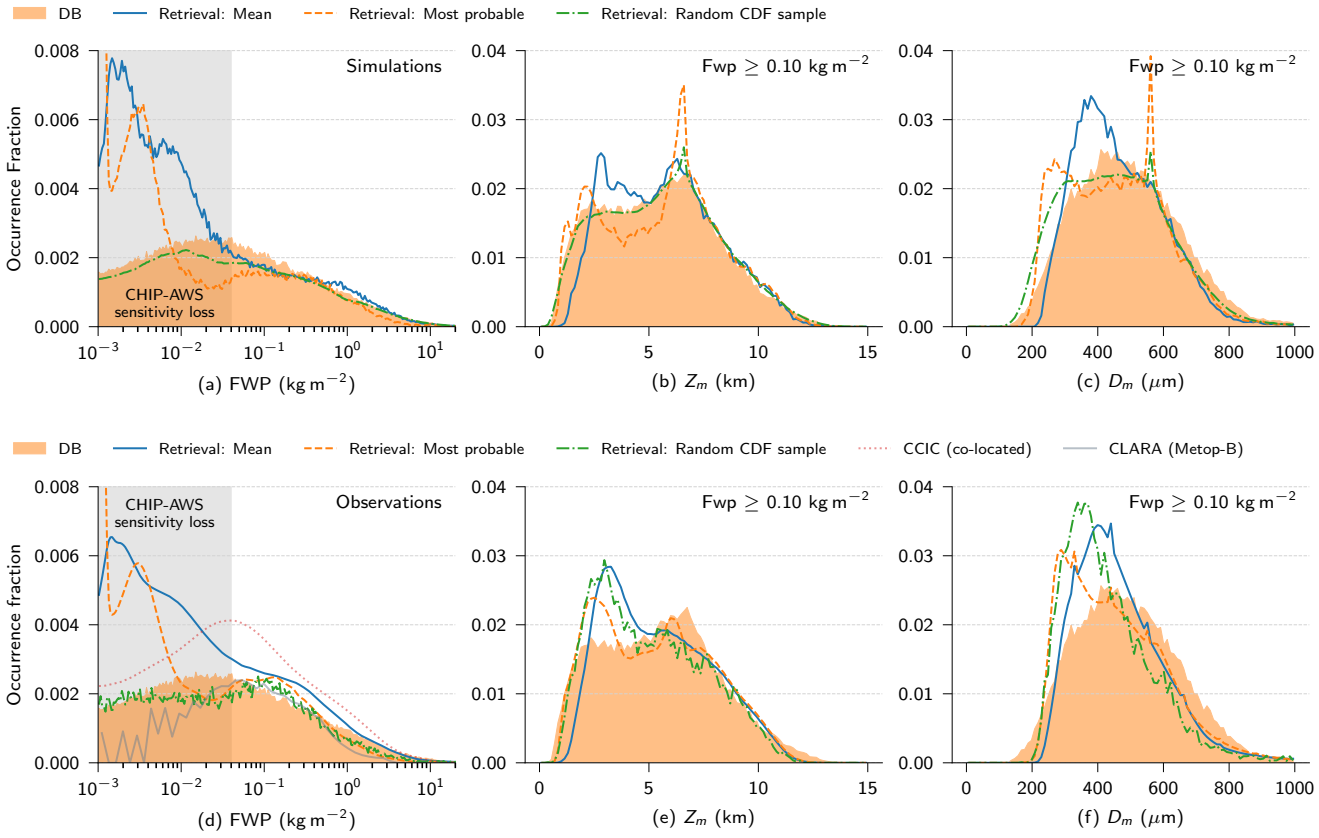


Figure 6. Occurrence fractions, i.e. binned value counts divided by total sample count. Top row **(a–c)** shows retrievals (mean and most-probable) on simulated T_a values from the test-subset of the simulation database with the filled region (DB) being the "true" database values. The "random sample" retrievals are obtained by taking a random sample according to the retrieved CDF. Bottom row **(d–f)** shows retrievals on actual observations. Co-located FWP values from CCIC and 2025 values from the CLARA record retrieved from Metop-B (ECT 09:31) are included for comparison. Same as in the top row, the filled region (DB) shows the distribution of "true" values from the test subset of the database and is included as a reference for the random CDF sampling.

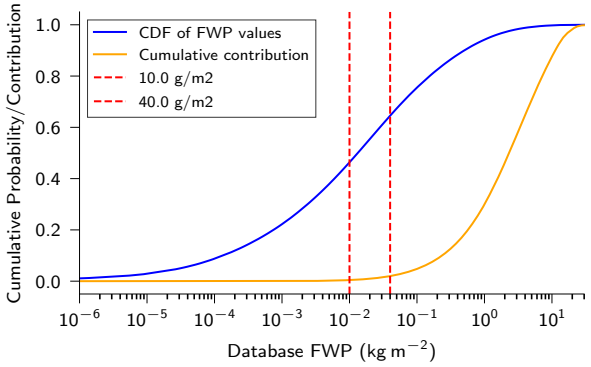


Figure 7. The cumulative distribution of reference FWP values and the cumulative contribution to the total FWP in the simulation database.

Related mass property retrievals for Z_m and D_m are more uncertain when FWP is low. As a consequence, Z_m and D_m values have been filtered to only include cases with significant FWP values, here the threshold of $0.1\,\mathrm{kg\,m^{-2}}$ has been found to remove uninformative estimates. For these estimates there is good agreement between the distribution of retrieved values and true values, although cases slightly below $5\,\mathrm{km}$ for Z_m and below $450\,\mu\mathrm{m}$ for D_m are overrepresented.

From retrieved CDFs, the mean estimate Eq. (8) and the most probable estimate Eq. (9) are computed. For these statistical overviews, the most-probable estimate follows the true occurrence fraction distribution but starts to deviate near the sensitivity limit. These estimates also exhibit a sharp peak of overrepresented values for Z_m at $7\,\mathrm{km}$ and for D_m at $600\,\mu\mathrm{m}$.

Additionally, retrieved CDFs can be randomly sampled and are expected to recreate the training data distribution (the prior). For FWP and Z_m the prior closely matches the underlying database, though with a slight underestimation of the number of samples for values below $1\,\mathrm{kg\,m^{-2}}$. For D_m, the prior is similarly close to the database distribution but shifted towards smaller values, with a peak at $600\,\mu\mathrm{m}$.

The impact of overestimating the occurrence of lower FWP values can be put into context with Fig. 7, which shows the cumulative distribution of reference FWP values in the simulation database and the cumulative contribution of FWP values to the total. This shows that values below $10\,\mathrm{g\,m^{-2}}$ and $40\,\mathrm{g\,m^{-2}}$ constitute about 50% and 60% of all cases, respectively, yet contribute negligibly to the total.

5.2.2 Conditional densities and variable correlations

Figure 8 shows conditional probability densities of retrieved estimates given the true values $p(\text{retrieved} \mid \text{true})$, together with their conditional mean $\mathbf{E}[\text{retrieved} \mid \text{true}]$ for the test subset of the database. For FWP, the conditional mean follows the 1:1 line closely from $10\,\mathrm{kg\,m^{-2}}$ down to values of $10\,\mathrm{g\,m^{-2}}$, below which retrievals tend upwards and overestimate the ice mass, indicating a loss of sensitivity. In this comparison the sensitivity is slightly better than, but consistent with, the occurrence fractions in Fig. 6a, where sensitivity started to degrade for values below $40\,\mathrm{g\,m^{-2}}$.

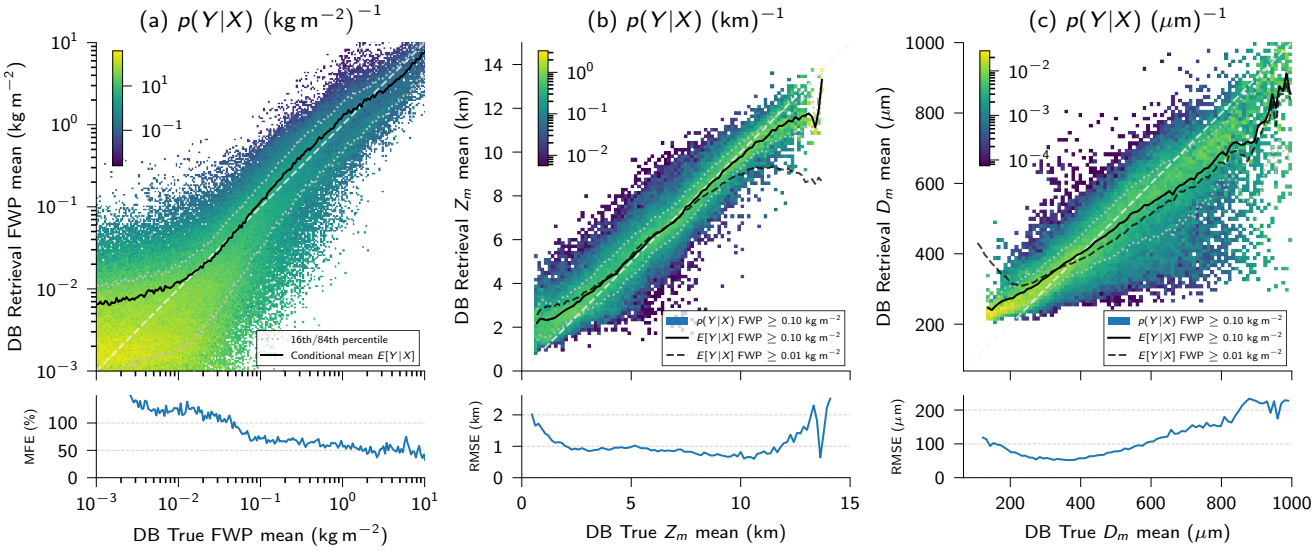


Figure 8. Conditional probability densities of FWP, Z_m, and D_m retrieved from T_a values from the test-subset of the simulation database (y-axis) conditioned on the true value from the database (x-axis), $p(y \mid x)$. Densities and conditional means for Z_m and D_m are computed with values corresponding to $\mathrm{FWP} \geq 0.1\,\mathrm{kg\,m^{-2}}$. An additional conditional mean is computed with values corresponding to $\mathrm{FWP} \geq 0.01\,\mathrm{kg\,m^{-2}}$ to show the impact of lower FWP on precision for these variables. The bottom row shows an error estimate for each respective quantity. For FWP, the error is expressed in median fractional error (MFE; Holl et al. 2014, median of Eq. 1), a metric more suitable to the exponential nature of the FWP values. For Z_m and D_m, the root mean square error (RMSE) of the retrievals (with $\mathrm{FWP} \geq 0.1\,\mathrm{kg\,m^{-2}}$) are plotted for each true database value.

The densities for Z_m and D_m, after being filtered for cases with $\mathrm{FWP} \geq 0.1\,\mathrm{kg\,m^{-2}}$, show agreement between retrieved estimates and true values. However, for D_m, estimates tend to overestimate particle sizes under 400 µm and underestimate the sizes above.

The threshold filtering is added due to estimates for Z_m and D_m being uninformative when observing cases with low mass-content. To demonstrate this, an additional conditional mean is added to the panels for Z_m and D_m computed with a lower threshold $\mathrm{FWP} \geq 0.01\,\mathrm{kg\,m^{-2}}$. With these extra low-FWP cases, the conditional mean shows that Z_m and D_m both overestimate and underestimate to a stronger degree.

In the bottom row of Fig. 8, two precision metrics are used: the median fractional error (MFE; Holl et al. 2014, median of Eq. 1) for FWP and the root mean square error (RMSE) for Z_m and D_m. For FWP, the MFE is $\sim 150\%$ at values of $10\,\mathrm{g\,m^{-2}}$, 75% or below at $100\,\mathrm{g\,m^{-2}}$, and below 50% at $1\,\mathrm{kg\,m^{-2}}$. These correspond to median errors of $2.5\times$, $1.75\times$, and $1.5\times$ the true value, respectively. For Z_m, RMSE remains below 1 km across the 2–12 km range. For D_m, RMSE varies between 50 and 200 µm.

FWP Threshold	$r_{(\mathrm{FWP})}$	r_{Z_m}	r_{D_m}
No Threshold	0.89	0.79	0.46
$> 10\,\mathrm{g\,m^{-2}}$	0.88	0.88	0.71
$> 100\,\mathrm{g\,m^{-2}}$	0.87	0.94	0.82

Table 4. Correlation coefficient between retrieved estimates and true values from the test subset of the simulation database. The correlations are calculated for cases with a true FWP value greater than that indicated in the table.

Dataset	$r_{(\mathrm{FWP},Dm)}$	$r_{(\mathrm{FWP},Zm)}$	$r_{(Dm,Zm)}$
$\mathrm{FWP} > 10\,\mathrm{g\,m^{-2}}$			
Training	0.38	0.01	-0.39
Test	0.48	0.02	-0.31
CHIP-AWS	0.39	0.04	-0.32
$\mathrm{FWP} > 100\,\mathrm{g\,m^{-2}}$			
Training	0.32	0.09	-0.25
Test	0.43	0.10	-0.28
CHIP-AWS	0.29	0.12	-0.28

Table 5. Correlation coefficient between the retrieval variables. The correlations are calculated only for cases with a FWP value greater than that indicated in the table. For the training set, the true values are used. For the test set, the correlation is computed between retrieved estimates, but the true FWP is used as a threshold. For the CHIP-AWS dataset (from actual observations), all values used are retrieved estimates.

Table 4 shows correlation coefficients between retrieved estimates and true values across three conditions: no threshold, and the same two FWP thresholds used in Fig. 8. FWP estimates correlate with true values at 0.87–0.89 across all conditions. As the FWP threshold increases, Z_m correlations range from 0.79 to 0.94, whilst D_m correlations range from 0.46 to 0.82.

Table 5 shows correlations between the retrieval variables themselves, also filtered with the FWP thresholds. The aim is to assess whether the correlations between variables are preserved in the retrievals, since there can be a tendency for predictions to overstate correlations if there is not enough information available in the observations to constrain both variables simultaneously. For the test subset of the database, correlations of FWP with Z_m or D_m are in some cases stronger in the retrievals than in the true values. However, the differences remain relatively small.

Although retrievals on real observations are not presented until Section 5.3 and onwards, we note here that their correlations agree even more closely with the training data than seen for the test subset, which is a promising result. No large changes in behaviour are observed as a result of changing FWP threshold.

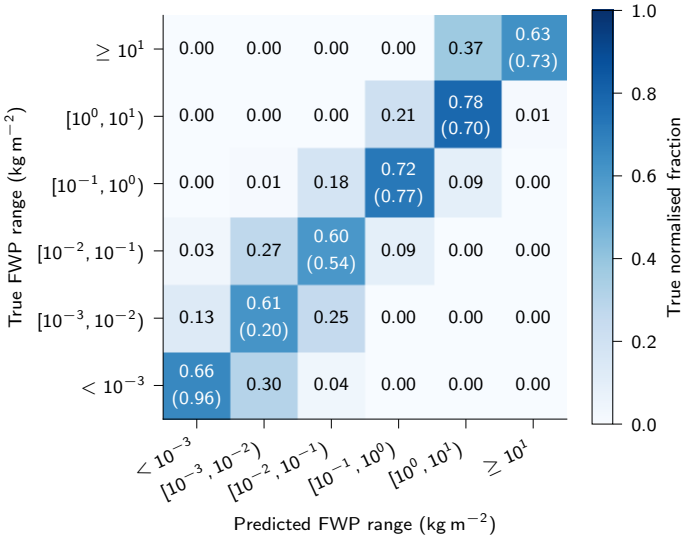


Figure 9. Confusion matrix comparing FWP estimates from simulated observations against reference values. Each row represents a true FWP range and is normalised to sum to one. Diagonal entries thus show the recall, i.e. the fraction of cases correctly estimated to fall within the range. In parentheses, the precision is shown, i.e. the fraction of FWP estimates within that range that are correct.

5.2.3 Confusion matrix

Figure 9 presents a confusion matrix in which FWP estimates and reference values are binned into magnitude ranges. Each row corresponds to a reference class and is normalised. The matrix shows good agreement between predicted and reference classes: approximately 60% of cases are correctly classified for lower FWP ranges (10^{-3}–$10^{-1}\,\mathrm{kg\,m^{-2}}$), while approximately 60–80% are correctly classified for higher FWP ranges.

Due to being row-normalised, each diagonal cell gives the recall, with precision added in parentheses. Recall is share of each reference class that is correctly estimated; precision is the share of all estimates in that range that are correct. For $[10^{-3}, 10^{-2})$, recall is 0.61 and precision is 0.20, indicating most estimates in this range belong to other classes. For clear-sky ($< 10^{-3}\,\mathrm{kg\,m^{-2}}$), recall is 0.66 and precision is 0.96, the high precision reflects the predominance of clear-sky cases in the database.

The confusion matrix reveals two patterns. First, extreme FWP values are not confused with each other: clear-sky cases are never estimated as having high FWP, and vice versa. Second, misclassifications occur almost exclusively between adjacent classes. This indicates that the retrievals do not produce spurious large FWP values. When the retrieval estimates substantial FWP a substantial amount of FWP is present.

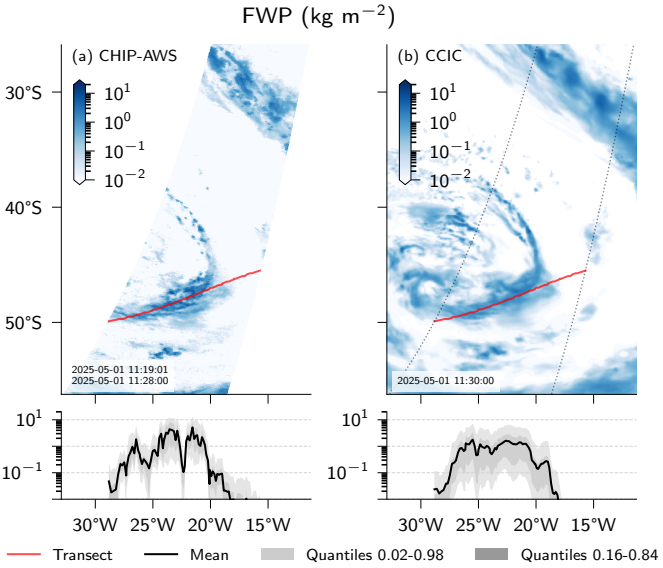


Figure 10. Comparison of real observations from the same scene between **(a)** CHIP-AWS and **(b)** CCIC. The top row shows the mean FWP estimate for each footprint. The bottom row shows estimates and uncertainties sampled along the transect line and projected onto the longitude axis. The transect traverses a large region with varying FWP values.

5.3 Retrieval performance on observations

5.3.1 Co-located comparisons with CCIC

Figure 10 presents a case-specific comparison between CHIP-AWS and CCIC, covering the same weather system. At the largest scale, both datasets capture the system's main features in overall shape, magnitude, and transect values, with tighter uncertainty bounds for CHIP-AWS, as seen in the bottom row. For medium scale structures, covering 4 footprint-pixels or more, CHIP-AWS resolves small but intense cores in the spiral arm at $45°$ S and $30°$ S that CCIC smooths out; similarly, the transect shows three distinct areas of elevated FWP values in CHIP-AWS that are not resolved in CCIC. The confusion matrix in Fig. 9 showed that high FWP are rarely confused with low FWP values. This suggests that the small high-FWP structures surrounded by low values seen in the scene represent real structure. At fine scales, CHIP-AWS exhibits variation and small intense values absent in CCIC, a difference attributed to CCIC using CNNs (resulting in correlated errors) whereas CHIP-AWS performs independent retrievals for each footprint.

A statistical comparison of co-located retrievals from CHIP-AWS and CCIC is presented in Fig. 11, where the probability density of co-located CCIC FWP estimates are conditioned on CHIP-AWS estimates. The conditional mean crosses the 1:1 line near $1\,\mathrm{kg\,m^{-2}}$. CCIC, on average, overestimates in the range 10^{-3} to $1\,\mathrm{kg\,m^{-2}}$ relative to co-located CHIP-AWS and underestimates above. This pattern matches that in Amell et al. (2024) (their Fig. 6, equivalent to our Fig. 8a), which shows

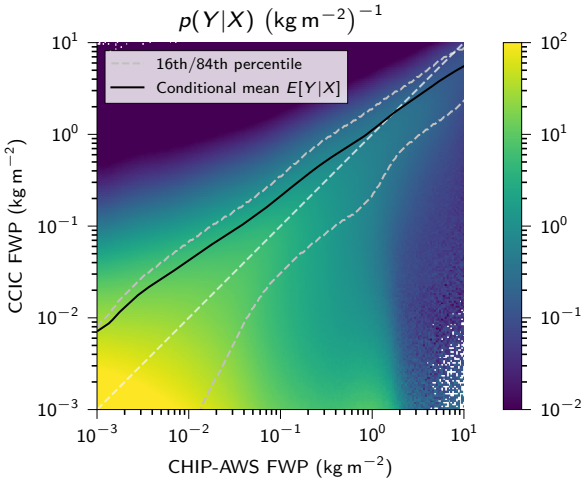


Figure 11. Conditional probability density function of co-located CCIC FWP mean estimates conditioned on CHIP-AWS FWP mean estimates. It is the probability of an observed CCIC FWP mean estimate given the corresponding CHIP-AWS mean estimate. The conditional mean $\mathbf{E}$[CCIC|CHIP-AWS] is also included.

a conditional PDF of CCIC retrievals conditioned on 2C-ICE values (CCIC's training data). There too, the conditional mean crosses the 1:1 line at $1\,\mathrm{kg\,m^{-2}}$, with a higher conditional mean for values below and a lower for values above. Even though CCIC is expected to be closer to its training data on average than CHIP-AWS, this result suggests that CHIP-AWS provides more accurate FWP estimates over a wider range of values than CCIC, when compared to 2C-ICE for individual retrievals. This is discussed further in Sect. 6.

5.3.2 Occurrence fractions

Figure 6d–f shows occurrence fraction plots of binned FWP, Z_m, and D_m estimates (mean and most-probable) retrieved from actual AWS measurements for 2025. Additionally, the figure includes the occurrence fraction of random samples from the retrieved CDF, expected to follow the database distribution (the prior). The database distribution serves as a rough reference rather than a direct benchmark.

The retrieval estimates from real measurements follow the expected occurrence distribution across a wide range of FWP values (from $10\,\mathrm{kg\,m^{-2}}$ down to $40\,\mathrm{g\,m^{-2}}$) and fall slightly below the CCIC distribution. This is a good result considering that they are estimates from passive observations, and that previous passive FWP datasets have struggled to follow the distribution over such a wide range (Wu et al., 2024, their Fig. 1). The related variables Z_m and D_m also follow the database distributions, with filtering ($\mathrm{FWP} \geq 0.1\,\mathrm{kg\,m^{-2}}$), though with a tendency to overestimate the frequency of lower values.

Comparing with occurrence fractions of retrievals performed on simulated observations (Fig. 6a–c), the real retrieval mean and most-probable estimates have a similar distribution and performance. For FWP, however, retrieved values between 0.04 and

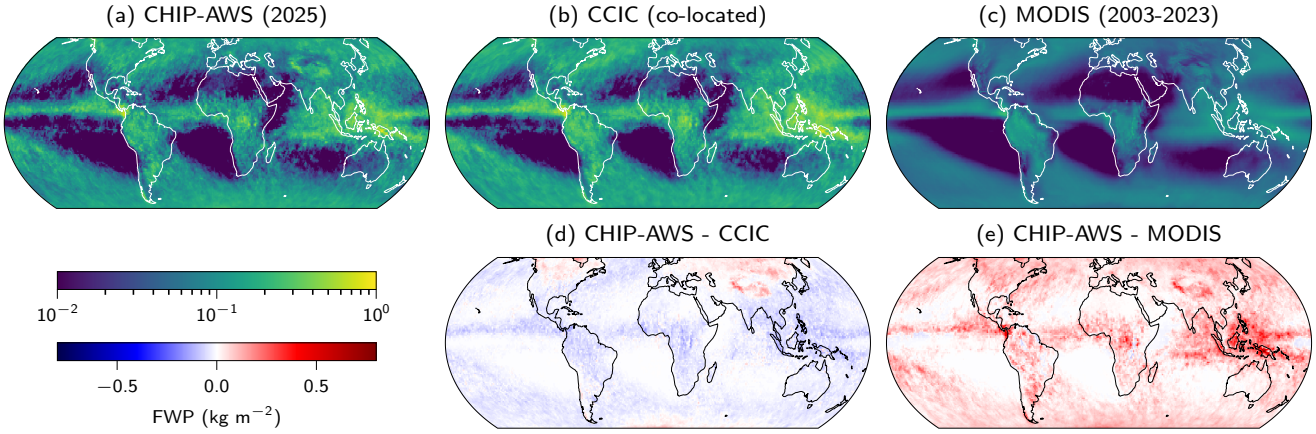


Figure 12. The local means (i.e. average spatial distribution) of FWP estimates binned and averaged at $1^\circ \times 1^\circ$ resolution for 2025 from **(a)** CHIP-AWS and **(b)** CCIC. CCIC retrievals are collocated with CHIP-AWS footprints from all of 2025. A longer-timescale comparison is provided by **(c)** MODIS cloud ice water path averaged over two decades (2003–2023). Panels **(d)** and **(e)** show the differences obtained by subtracting CCIC and MODIS, respectively, from the 2025 CHIP-AWS estimates.

$1\,\mathrm{kg\,m^{-2}}$ are slightly more frequent than those retrieved from the simulated T_a values. This discrepancy may reflect differences in retrieval performance when applied to real observations versus simulated values. Alternatively, it may be due to measuring different atmospheric conditions. AWS and CloudSat follow different orbits, causing them to sample at different local times of day. Additionally, differences between 2015 and 2025 may also contribute.

For comparison, estimates from two other passive FWP retrievals are included: co-located CCIC and 2025 CLARA-A3 estimates (Karlsson et al., 2023a) from Metop-B that has an equatorial crossing time of 09:31, similar to AWS's at roughly 10:30. However, CLARA's retrievals operate only during morning passes, whereas CHIP-AWS operates during both morning and evening passes. CHIP-AWS and CCIC show good agreement at the highest FWP values. Below, CHIP-AWS gives fewer cases than CCIC until it appears to lose sensitivity at $40\,\mathrm{g\,m^{-2}}$. CLARA underestimates the number of high FWP values compared to the database, CCIC and CHIP-AWS.

The random CDF sample estimates are expected to recreate the database distribution. This holds for FWP down to the sensitivity limit. For Z_m and D_m, a peak at lower values deviates from the database distribution.

5.3.3 Local means

Figure 12 shows the local means (average spatial distribution) of FWP estimates from CHIP-AWS and CCIC (co-located) for the year 2025, averaged estimates from MODIS (2003–2023), as well as the difference between them. Apart from orographic cloud formation, the CHIP-AWS estimates show no coastline artefacts. This indicates that, even though simulations over land did not achieve as close a match in distribution of simulated T_a for lower and more rare values as over the ocean (Sect. 5.1), the

trained model still generalizes over the two regimes and produces reasonable estimates, with one major exception: dry cases over snow or ice, where the retrieval method struggles.

Looking at the difference between CHIP-AWS and CCIC (Fig. 12d), clear artefacts of overestimated values are apparent over Tibet in Asia, Hudson Bay and the Saint Elias Mountains in North America, as well as general snow-cover and sea ice towards Antarctica. This has been attributed to incorrect assumptions on surface snow and ice emissivities used in the simulations for the new sub-millimetre frequencies. The dataset provides surface type fractions for each observation, allowing users to filter out cases with snow or sea ice. In other areas, CHIP-AWS tends to estimate lower FWP values than CCIC. This is expected and echoes the result from the conditional PDF with CCIC (Sect. 5.3.1), where CCIC tends to estimate higher values than CHIP-AWS for the same measurements. Comparing with MODIS (Fig. 12c,e), CHIP-AWS values are consistently higher.

5.3.4 Zonal means

Figure 13 shows the average FWP estimates binned by latitude for 2025, alongside the Z_m and D_m estimates. We compare these with historical data from the CloudSat- and CALIPSO-derived DARDAR dataset for 2007–2010, which include both morning and evening observations. After 2010, the cloud radar was deactivated for evening passes to address power issues. FWP values from CCIC co-located with CHIP-AWS are also included for comparison and can serve as a proxy for 2C-ICE estimates, another CloudSat- and CALIPSO-derived dataset.

Before comparing, it should be noted that between 2C-ICE and DARDAR, two independent cloud property retrievals using the same instruments, there is a 20% difference in such zonal mean values (Eriksson et al., 2026). Although cloud radar and lidar retrievals are expected to provide the best available benchmarks, considerable uncertainty remains about the true values. A close agreement in shape between CHIP-AWS and CCIC is expected, since both datasets sample from the same atmospheric conditions due to being co-located here.

The CHIP-AWS FWP zonal mean closely follows the shape of the CCIC values, suggesting a near-constant ratio between them, though CCIC values are biased higher compared to CHIP-AWS. Between CHIP-AWS and CCIC there are latitude-weighted mean differences of -0.020, -0.026, and $-0.010\,\mathrm{kg\,m^{-2}}$ for southern mid-latitudes, tropics, and northern mid-latitudes, respectively.

Comparing with DARDAR, the CHIP-AWS dataset aligns more closely than CCIC in the tropics, with a latitude-weighted mean difference of $-0.008\,\mathrm{kg\,m^{-2}}$ compared to CCIC's $0.018\,\mathrm{kg\,m^{-2}}$. For the mid-latitudes both CHIP-AWS and CCIC are close to DARDAR, with CHIP-AWS showing a difference of $-0.012\,\mathrm{kg\,m^{-2}}$.

Near the dataset's latitudinal bounds ($\pm 60°$), CHIP-AWS FWP estimates increase above both CCIC and DARDAR, attributable to poor retrieval performance for dry cases over ice and snow. Other passive FWP estimates are also shown: MODIS for 2003–2023 and CLARA for 2025 (from Metop-B). Both fall substantially below DARDAR, CCIC and CHIP-AWS. That these passive retrievals fall below radar retrievals is consistent with previous findings (Eliasson et al., 2011; Duncan and Eriksson, 2018) and reflects the limited information content that these sensors can extract from deeper within clouds.

For Z_m, our estimates match the DARDAR zonal mean, with a slight positive difference ranging between 0.5–$0.7\,\mathrm{km}$ across zonal regions. For Z_m, radar-lidar retrievals are expected to be a precise reference for non multi-layer cloud cases.

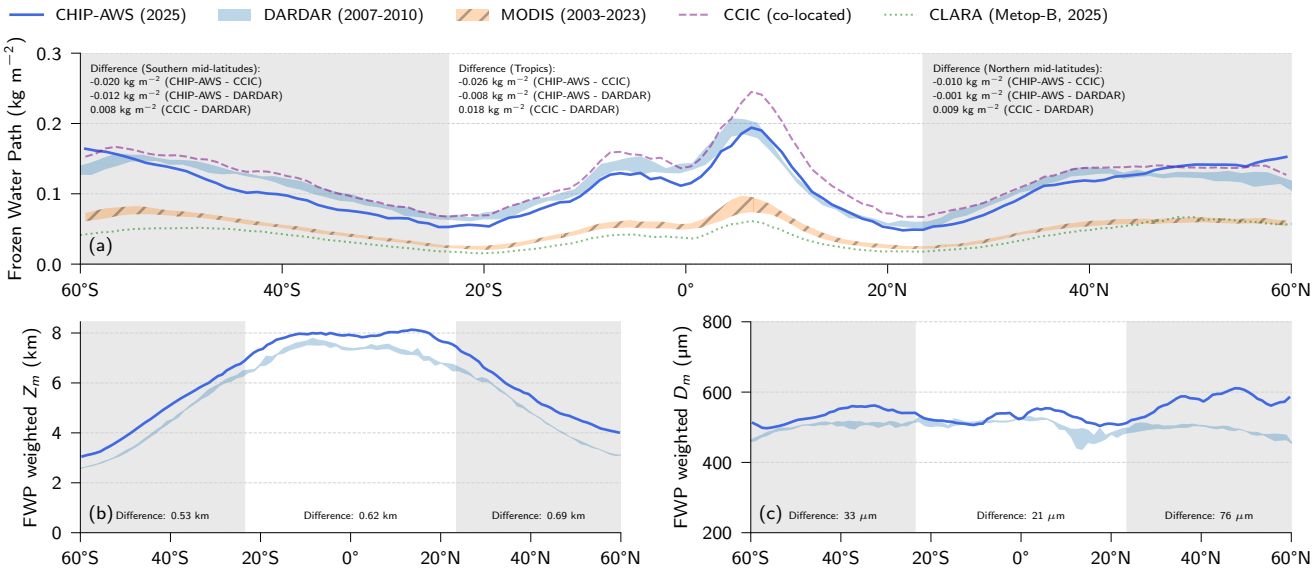


Figure 13. Zonal means of retrieved quantities from CHIP-AWS for 2025, binned by latitude. Z_m and D_m values are weighted by their corresponding FWP estimates, as these retrievals represent mass-weighted averages. For comparison, retrievals from CCIC, DARDAR, MODIS, and CLARA are also shown. CCIC has been co-located to the AWS footprints, enabling direct FWP comparison. DARDAR allows historical comparison across all variables: FWP, Z_m, and D_m. MODIS and CLARA provide additional FWP comparisons from independent passive retrieval records. Metop-B retrievals from CLARA are selected for 2025 to match the current CHIP-AWS record, as its equatorial crossing time closely matches that of AWS. Note, however, that CLARA provides retrievals for the descending pass only. Both DARDAR and MODIS show interannual spread as filled area.

For D_m, our estimates are compared to DARDAR retrieved values. However, before comparison, we note that DARDAR's particle diameter is expressed as melted equivalent diameter d_{meq}, while we retrieve volume equivalent diameter d_{veq}. We convert radar estimates as $d_{\mathrm{veq}} = d_{\mathrm{meq}} \left(\frac{\rho_{\mathrm{water}}}{\rho_{\mathrm{ice}}} \right)^{1/3}$. Our D_m estimates overestimate sizes for northern mid latitudes. Compared to DARDAR, the CHIP-AWS estimates show latitude-weighted mean difference of 33, 21, and 76 µm for southern mid-latitudes, tropics and northern mid-latitudes, respectively. However, here, radar-lidar retrievals have limitations with respect to sensing particle sizes (see introduction). The combination of channels offered by AWS have the potential to constrain D_m better (Pfreundschuh et al., 2020), but this benefit is difficult to validate.

Figure 14 presents a Hovmöller diagram showing temporal variability in FWP and Z_m through zonal means averaged with a 3-week rolling window. The diagram reveals clear seasonal movement of the ITCZ. It also shows increased FWP poleward of 40° N/S during local winter whilst Z_m decreases. This demonstrates that the dataset captures expected seasonal variability across the year. This is notable, since the retrieval model receives no information about time or location.

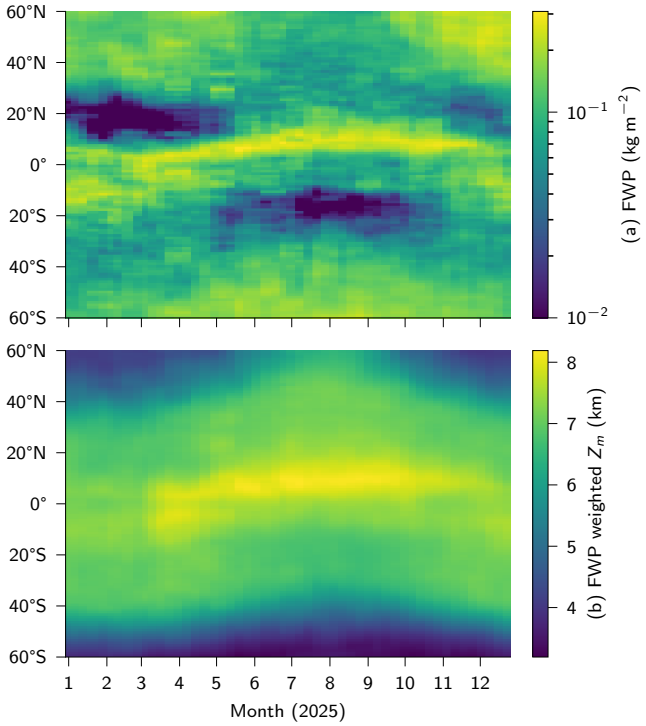


Figure 14. Hovmöller diagram (the zonal mean over time) of retrieved **(a)** FWP estimates and **(b)** Z_m weighted by FWP. Values are binned into latitudes for every week of the year and then averaged over time with a rolling three week window.

5.3.5 Across-track dependence

Figure 15 shows the deviation of the mean for each field-of-view (scan angle) from the overall mean of all retrieved estimates for 2025. This indicates a small scan-dependent increase for FWP and Z_m; a change of $1\,\mathrm{g\,m^{-2}}$ and $200\,\mathrm{m}$, respectively, across the swath. D_m estimates shows a more clear scan-dependent behaviour across the swath. A cyclic pattern is seen in the deviations for all variables. The remap distance subplot hints that this is due to the re-interpolation process (Sect. 2.1). Still, this observed field-of-view dependence and cyclic behaviour is negligible compared to the sensitivity limits identified in Sect. 5.2 ($10\,\mathrm{g\,m^{-2}}$ or $40\,\mathrm{g\,m^{-2}}$) and can be ignored.

6 Discussion

Synthetic retrievals performed on simulated instrument measurements were used to characterise the retrieval performance. Precision metrics (MFE and RMSE) from these comparisons showed 75 % MFE and below for FWP above $0.1\,\mathrm{kg\,m^{-2}}$ and 50 % for FWP above $1.0\,\mathrm{kg\,m^{-2}}$, $\leq 1\,\mathrm{km}$ RMSE for Z_m between 2–12 km, and RMSE varying between 50 and 200 µm for D_m. Since no FWP MFE metrics are reported for MODIS, CLARA or DARDAR, we put our results into context with

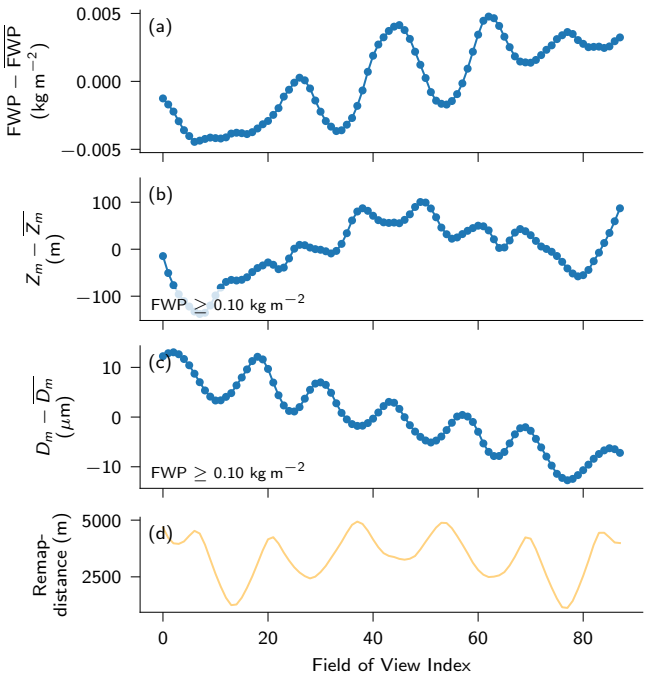


Figure 15. Per field-of-view deviation from the overall 2025 annual mean for **(a)** FWP, **(b)** Z_m, and **(c)** D_m, illustrating the magnitude of any field-of-view-dependent differences. Panel **(d)** shows the per field-of-view remap-distance between AWS channel footprints for the re-interpolation process.

reported metrics from SPARE-ICE (Holl et al., 2014), a passive FWP retrieval method from combined microwave and infrared measurements. SPARE-ICE achieves an MFE for FWP relative to its reference of about 100% for values below $1\,\mathrm{kg\,m^{-2}}$. The MFE decreases to 75% and 50% MFE for values above (Holl et al., 2014, their Fig. 7). Thus, CHIP-AWS achieves a similar 75% MFE at a lower threshold of $0.1\,\mathrm{kg\,m^{-2}}$. However, SPARE-ICE maintains a 100 % MFE for values down to $1\,\mathrm{g\,m^{-2}}$ likely thanks to the IR information that is more sensitive to smaller particles, whereas CHIP-AWS's MFE increases to about 250 % for the same values.

Simulated retrievals also provided correlation coefficients (Table 4) of 0.89, 0.79, and 0.46 for FWP, Z_m, and D_m respectively, without applying an FWP threshold to Z_m and D_m. These metrics compare favourably for FWP and Z_m with the equivalent correlations in May et al. (2024, Fig. 9), where a similar FWP retrieval product is developed for the upcoming Ice Cloud Imager with sub-millimetre channels at 325 and 664 GHz. Their synthetic retrievals achieve correlations of 0.86, 0.75 and 0.83 for FWP, Z_m, and D_m respectively. The FWP and Z_m correlations are similar across both, though D_m shows notably stronger correlation in the Ice Cloud Imager retrievals than in CHIP-AWS.

The strong agreement between simulated and observed T_a values presented (Fig. 4 and Fig. 5) is a prerequisite for the retrieval characterisations made on synthetic data, such as the conditional PDF (Fig. 8), to extend to real observations. Still, the

method behind the simulations has aspects that can be improved. A melting layer is not currently present in the simulations, due to lacking scattering data for melting particles. There can be inconsistencies between the ERA5 data and CloudSat data, where high FWP is reported yet with a low relative humidity. We have also identified that, over land, some intense tropical deep convection causes situations that our simulations struggle to recreate. Tropical deep convection over land creates large ice hydrometeors, likely not represented well enough by current particle models. Finally, the treatment of ice and snow surface emissivity and adapting them to the new sub-millimetre frequencies is currently the largest limitation in the simulations.

For comparing actual retrievals, we would ideally validate against co-located radar retrievals. CloudSat was decommissioned in 2023, eliminating this option. EarthCARE (launched 2024) and the ACM-CAP (Mason et al., 2023) dataset could be used, but this remains under active development with no stable official retrievals available at the time of writing. Moreover, we have verified that EarthCARE has no co-locations with AWS outside of the polar regions. We therefore had to compare against historical datasets and other passive retrievals.

In the zonal mean comparisons (Fig. 13), CHIP-AWS achieves good agreement with historical DARDAR data. Previous machine-learning approaches trained on radar retrievals similarly outperform passive retrievals in terms of zonal mean values (Yang et al., 2026; Amell et al., 2024), here represented by CCIC. Other passive retrievals, however, show strong underestimation of mean FWP values, consistent with previous studies (Eliasson et al., 2011; Duncan and Eriksson, 2018).

CCIC is currently the only dataset allowing substantial co-location with AWS. The probability density of CCIC estimates conditioned on CHIP-AWS estimates (Fig. 11) showed a varying difference across the FWP range, as seen in the shape of the conditional mean relative to the 1:1 line. Notably, this conditional mean recreates that between CCIC conditioned on its training data, 2C-ICE (Amell et al., 2024, their Fig. 6). This similarity suggests that CHIP-AWS is more consistent with 2C-ICE, for individual retrievals. One explanation for this better performance is that CCIC is limited to one IR channel at $11\,\mu\mathrm{m}$ for its FWP information, while CHIP-AWS has 11 microwave and sub-millimetre channels. This consistency with 2C-ICE indicates that the strong synthetic validation results extend to real observations to some degree.

Together, these results demonstrate good performance characteristics and provide the practically achievable validation that these characteristics extend to real observations. This dataset represents a passive retrieval method of FWP, Z_m, and D_m with added accuracy over a wide dynamic range, and zonal means comparable to cloud profiling radars. It provides broad spatial coverage that only passive instruments can provide, making it a valuable complement to existing passive and active retrievals.

7 Conclusions

The first version of the "Chalmers Hydrometeor Inversion Product from the Arctic Weather Satellite" (CHIP-AWS) is introduced. This dataset provides estimates of frozen water path (FWP), mass-weighted mean altitude Z_m, and mass-weighted mean particle volume-equivalent diameter D_m. These estimates are retrieved from antenna temperature (T_a) values measured by AWS's across-track scanning radiometer, which features novel sub-millimetre channels. This marks the first regular dataset utilising improvements that operational sub-millimetre observations can offer to ice hydrometeor property retrievals. The data

product begins in January 2025 and is regularly expanded as more AWS data become available; an archival copy of 2025 retrievals is also published (see the data availability section).

The retrieval method employs QRNNs, which provide per-retrieval uncertainties in terms of quantiles. Training data were generated through rigorous radiative transfer simulations, yielding a physics-based database. This approach was necessitated by the absence of any prior Earth-facing sub-millimetre data with broad geographical coverage. Radiative transfer simulations also offer the advantage of making all physical assumptions explicit, enabling new insights into cloud microphysics. A key limitation of simulation-based training data is that erroneous assumptions can affect retrievals.

Over ocean, simulated T_a distributions agree with their climatological counterpart observed over one year within latitudes 60° N/S. Over land, intense tropical deep convection causes very low observed T_a values not captured by the simulations. Ice- and snow-covered surfaces in dry or high-altitude regions cause the most significant discrepancies. Users of the dataset should consider using the provided surface type fractions to filter retrievals according to their use-case.

CHIP-AWS achieves independent agreement with the zonal mean of radar-lidar based retrievals from DARDAR (Cazenave et al., 2019) for all three variables: FWP, Z_m, and D_m. This is, to the best of our knowledge, the first passive retrieval method based on atmospheric radiative transfer simulations to do so (Duncan and Eriksson, 2018; Eriksson et al., 2026).

Results indicate that the retrieval method achieves negligible bias in FWP over a wide range, from $10\,\mathrm{kg\,m^{-2}}$ down to $10\,\mathrm{g\,m^{-2}}$ or $40\,\mathrm{g\,m^{-2}}$, depending on the comparison criteria. A strong result for passive retrievals. The estimates also show good precision: 75% MFE for values above $0.1\,\mathrm{kg\,m^{-2}}$ for FWP; RMSE below $1\,\mathrm{km}$ for Z_m (for 2–12 km when $\mathrm{FWP} \geq 0.1\,\mathrm{kg\,m^{-2}}$); and RMSE between 50 and 200 $\mu\mathrm{m}$ for D_m (when $\mathrm{FWP} \geq 0.1\,\mathrm{kg\,m^{-2}}$).

This performance is achieved whilst providing a swath of 800 km, substantially wider than the $1\,\mathrm{km}$ swath of cloud profiling radars. Because AWS's instrument is more directly sensitive to ice mass than CCIC's single IR channel, CHIP-AWS provides more precise local-scale estimates with higher horizontal resolution.

Ongoing work aims to improve the performance over ice and snow, extend latitudinal coverage from 60° N/S to global coverage, and expand the scan angle to increase the swath size. A future version of the dataset will also include level 2 data aggregated into a gridded level 3 dataset to facilitate analysis. Retrievals will also be extended to estimate vertical profiles of frozen water content (FWC) and D_m, following May and Eriksson (2025). Validation will be strengthened through comparison with EarthCARE-based retrievals and co-locations near the polar regions.

Related avenues one can explore further include ground-based sensor networks such as ACTRIS Cloudnet (Finnish Meteorological Institute, 2011), representing a source for co-located measurements for further validation. The new sub-millimetre channels also offer opportunities to perform super-cooled liquid water and snowfall retrievals, as suggested by simulation studies by Camplani et al. (2024).

We conclude by noting that this work and future developments are directly applicable to EPS-Sterna, a confirmed constellation of AWS satellites with a 13-year mission duration beginning in 2029. This work is also relevant to the Ice Cloud Imager (ICI) onboard the Metop-SG-B satellites, which is sensitive to sub-millimetre frequencies up to $664\,\mathrm{GHz}$. The first Metop-SG-B satellite is scheduled for launch in 2027. We aim to develop consistent retrievals for both ICI and the EPS-Sterna radiometers.

These missions will support each other by increasing coverage and providing cross-reference measurements in multiple ways. First, the two instruments have different scanning geometries: AWS uses an across-track scanner while ICI is a conically scanning instrument, and these complementary views can help constrain particle model assumptions. Second, ICI measures polarisation in both H and V, yielding richer information on particle properties and orientation. Insights can be incorporated into the simulation assumptions, improving retrievals for both instrument types. Together, they will provide an extensive record of sub-millimetre data well suited for ice mass property retrievals extending to 2045.

Data availability. An archival copy of 2025 retrievals used throughout this article can be accessed from the Swedish National Data Service under data DOI https://doi.org/10.71870/v9dx-rm43 (McEvoy, May, and Eriksson, 2026). Data from 2025 and onwards are continuously processed and made available at http://clouds-and-precip.group/datasets/chip-aws. The processor version corresponding to this publication is `chip-aws-v1.0.0`.

Input AWS Level 1b data is distributed by EUMETSAT under collection id `EO:EUM:DAT:0905` (EUMETSAT, 2024). The level-3 MODIS Atmosphere Daily global product is available from https://atmosphere-imager.gsfc.nasa.gov/products/daily (last access: 14 September 2026; Platnick and M. King 2017b, a). CLARA-A3 is available from EUMETSAT CM SAF (Karlsson et al., 2023a). DARDAR-CLOUD v3-10 data are available at the ICARE Data and Services Center (Delanoë and Hogan, 2025).

Author contributions. All authors contributed to the development of the database generation and retrieval framework. PE and EM provided input on all results and contributed to revisions of the paper. PM led the writing of the paper and performed the data processing, visualisation, and analysis of the results.

Competing interests. The authors have no competing interests to declare.

Acknowledgements. We are grateful to the four anonymous reviewers for their detailed comments, which helped us clarify key arguments. This work on AWS by PE, EM and PM is supported by the Swedish National Space Agency grants 2021-00077 and 2023-00139.

Appendix A: Antenna temperature distributions over surface types

As mentioned in Sect. 5.1, over land, the distribution of simulated T_a values does not perfectly match the distribution of observed T_a. Figure A1 shows the T_a distributions of simulations and observations decomposed into the different surface types: all, ocean, land, and a combined category of snow, ice, and glacier.

Over land there is a discrepancy for the channels with altitude sensitivity closest to the surface, AWS 31 (165.5 GHz) and even more so for AWS21 (89 GHz). For AWS 31, the simulated T_a values cover the range of all observed values, but underestimate the number of cases for values above 160 K. For AWS 21, simulated values only go down to 200 K, while observations show values down to 120 K. That some T_a values are simulated less frequently than observed is not ideal, but can be handled since simulations producing these values do exist. More problematic is when observed values ranges are not covered at all by simulations, as is the case for AWS21. The differences observed here have been attributed to unhandled surface effects, particularly for frozen (but non snow- or ice-covered) land and for certain cloud microphysics for very intense convection observed over land. This will impact retrieval performance for these cases.

For snow, ice, and glacier, there is a bigger problem. Here the distributions suggest shifted values, giving non-matching value ranges between simulations and observation for all channels except for AWS41 and AWS36. These simulated values all have a negative bias compared to observed values, causing values to be outside of the range of values seen in the observations. Since more channels have this discrepancy, the retrievals will be strongly impacted, especially when in dry atmospheric conditions or high altitude surfaces, where surface effects impact more. These artefacts are seen in the spatial distribution plot (Fig. 12, Sect. 5.3). This mismatch between observations and simulations is attributed to incorrect assumptions on surface reflectivities for snow and ice.

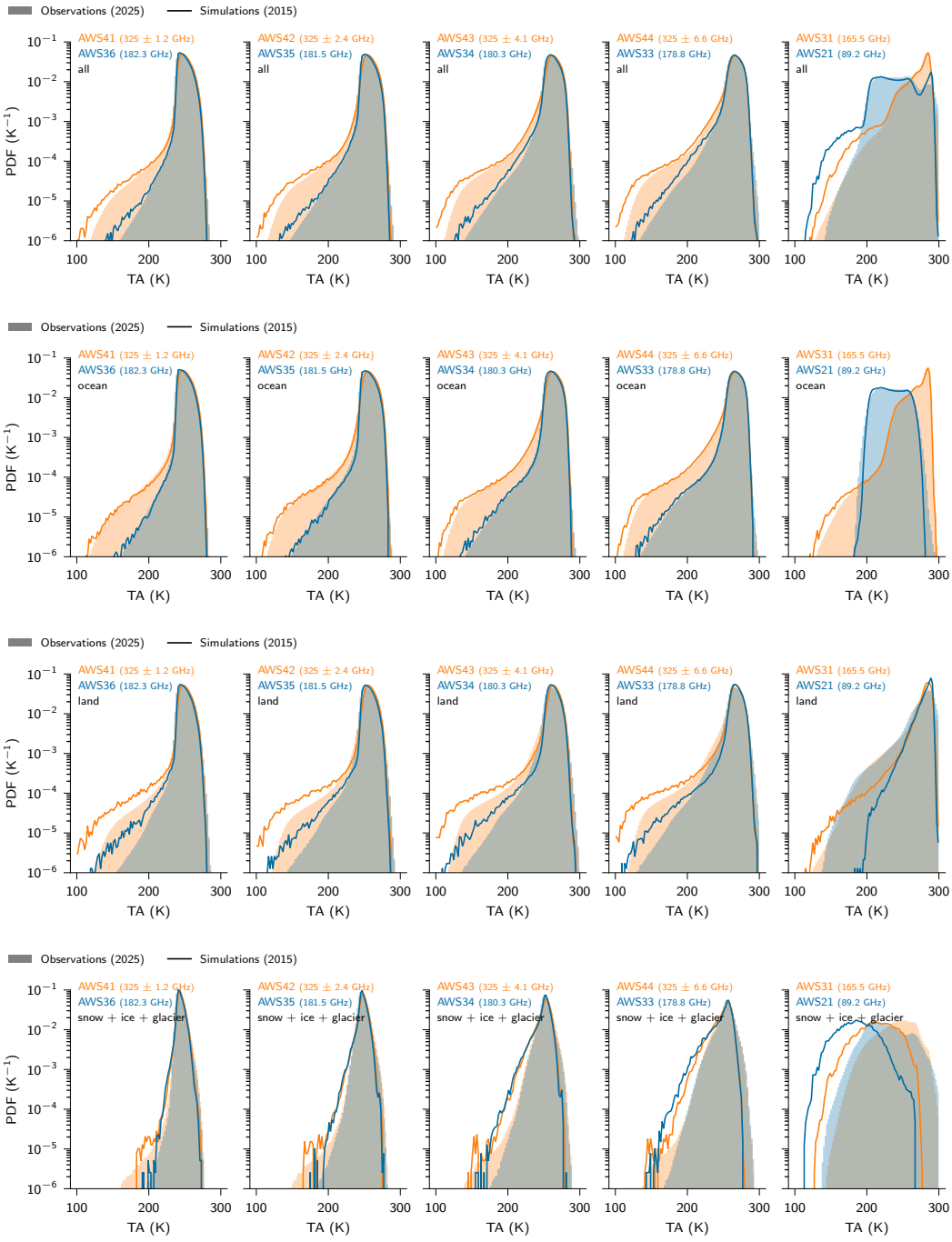


Figure A1. Distributions of simulated database T_a values (driven by CloudSat radar reflectivities from 2015) are shown as lines, whilst distribution of observed T_a values from AWS 2025 are shown as filled regions. Channels with similar altitudes of peak humidity sensitivity are paired together in the figure.

Latitude zone	Median	Q75	Q95
30°–60° N	24 h	143 h	168 h
0°–30° N	24 h	168 h	189 h
0°–30° S	24 h	164 h	189 h
30°–60° S	24 h	120 h	164 h

Table B1. Zonal medians of dataset revisit time statistics (descending only) for April – August 2025.

Appendix B: Revisit-time analysis

The revisit time analysis uses level 2 data from April to August 2025, excluding scans with bad quality flags. Only descending passes are included.

A grid of equal-area latitude-longitude cells of 50 km is established. For each satellite pass, observations and their timestamps are binned into these cells. A pass contributes no data to a bin if fewer than three observations fall within it.

For each bin, only observations separated by more than 30 minutes are retained to avoid counting multiple measurements from the same pass. Basic statistics for the time differences are then calculated.

These statistics reflect both the satellite's orbital behaviour and data processing effects, including data gaps and quality assurance filtering. See Table B1 and the supplemental material for the analysis code.

References

Amell, A., Eriksson, P., and Pfreundschuh, S.: Ice water path retrievals from Meteosat-9 using quantile regression neural networks, Atmospheric Measurement Techniques, 15, 5701–5717, https://doi.org/10.5194/amt-15-5701-2022, 2022.

Amell, A., Pfreundschuh, S., and Eriksson, P.: The Chalmers Cloud Ice Climatology: retrieval implementation and validation, Atmos. Meas. Tech., 17, 4337–4368, https://doi.org/10.5194/amt-17-4337-2024, 2024.

Bennartz, R. and Wu, D. L.: NASA's Polarized Submillimeter Ice-Cloud Radiometer (PolSIR): Observing the Diurnal Cycle of Ice Clouds in the Tropics and Sub-Tropics, in: 105th Annual AMS Meeting, vol. 105, p. 446951, https://doi.org/10.5194/egusphere-egu24-5886, 2025.

Bjordal, J., Storelvmo, T., Alterskjær, K., and Carlsen, T.: Equilibrium climate sensitivity above 5 °C plausible due to state-dependent cloud feedback, Nature Geoscience, 13, 718–721, https://doi.org/10.1038/s41561-020-00649-1, 2020.

Bony, S., Stevens, B., Frierson, D. M. W., Jakob, C., Kageyama, M., Pincus, R., Shepherd, T. G., Sherwood, S. C., Siebesma, A. P., Sobel, A. H., Watanabe, M., and Webb, M. J.: Clouds, circulation and climate sensitivity, Nature Geoscience, 8, 261–268, https://doi.org/10.1038/ngeo2398, 2015.

Buchhorn, M., Smets, B., Bertels, L., Roo, B. D., Lesiv, M., Tsendbazar, N.-E., Herold, M., and Fritz, S.: Copernicus Global Land Service: Land Cover 100m: collection 3: epoch 2019: Globe, https://doi.org/10.5281/zenodo.3939050, 2020.

Buehler, S. A., Defer, E., Evans, F., Eliasson, S., Mendrok, J., Eriksson, P., Lee, C., Jiménez, C., Prigent, C., Crewell, S., Kasai, Y., Bennartz, R., and Gasiewski, A. J.: Observing ice clouds in the submillimeter spectral range: the CloudIce mission proposal for ESA's Earth Explorer 8, Atmos. Meas. Tech., 5, 1529–1549, https://doi.org/10.5194/amt-5-1529-2012, 2012.

Buehler, S. A., Larsson, R., Lemke, O., Pfreundschuh, S., Brath, M., Adams, I., Fox, S., Roemer, F. E., Czarnecki, P., and Eriksson, P.: The atmospheric radiative transfer simulator ARTS, version 2.6 — Deep python integration, J. Quant. Spectrosc. Radiat. Transfer, 341, 109 443, https://doi.org/10.1016/j.jqsrt.2025.109443, 2025.

Camplani, A., Sanò, P., Casella, D., Panegrossi, G., and Battaglia, A.: Arctic Weather Satellite Sensitivity to Supercooled Liquid Water in Snowfall Conditions, Remote Sensing, 16, https://doi.org/10.3390/rs16224164, 2024.

Cazenave, Q., Ceccaldi, M., Delanoë, J., Pelon, J., Groß, S., and Heymsfield, A.: Evolution of DARDAR-CLOUD ice cloud retrievals: new parameters and impacts on the retrieved microphysical properties, Atmospheric Measurement Techniques, 12, 2819–2835, https://doi.org/10.5194/amt-12-2819-2019, 2019.

Delanoë, J. and Hogan, R. J.: DARDAR-cloud V3-10 [data set], AERIS/ICARE Data and Services Center, https://doi.org/10.25326/449, last access: 2 September 2025, 2025.

Delanoë, J. M. E., Heymsfield, A. J., Protat, A., Bansemer, A., and Hogan, R. J.: Normalized particle size distribution for remote sensing application, Journal of Geophysical Research: Atmospheres, 119, 4204–4227, https://doi.org/10.1002/2013JD020700, 2014.

Deng, M., Mace, G. G., Wang, Z., and Berry, E.: CloudSat 2C-ICE product update with a new Ze parameterization in lidar-only region, Journal of Geophysical Research: Atmospheres, 120, 12,198–12,208, https://doi.org/10.1002/2015JD023600, 2015.

Duncan, D. I. and Eriksson, P.: An update on global atmospheric ice estimates from satellite observations and reanalyses, Atmos. Chem. Phys., 18, 11 205–11 219, https://doi.org/10.5194/acp-18-11205-2018, 2018.

Earth Resources Observation and Science Center: Global 30 Arc-Second Elevation (GTOPO30), https://doi.org/10.5066/F7DF6PQS, 2018.

Ekelund, R., Eriksson, P., and Pfreundschuh, S.: Using passive and active observations at microwave and sub-millimetre wavelengths to constrain ice particle models, Atmos. Meas. Tech., 13, 501–520, https://doi.org/10.5194/amt-13-501-2020, 2020.

Eliasson, S., Buehler, S. A., Milz, M., Eriksson, P., and John, V. O.: Assessing observed and modelled spatial distributions of ice water path using satellite data, Atmos. Chem. Phys., 11, 375–391, https://doi.org/10.5194/acp-11-375-2011, 2011.

Eliasson, S., Holl, G., Buehler, S., Kuhn, T., Stengel, M., Iturbide-Sanchez, F., and Johnston, M.: Systematic and random errors between collocated satellite ice water path observations, J. Geophys. Res., 118, 2629–2642, https://doi.org/10.1029/2012JD018381, 2013.

Eriksson, P., Rydberg, B., Sagawa, H., Johnston, M. S., and Kasai, Y.: Overview and sample applications of SMILES and Odin-SMR retrievals of upper tropospheric humidity and cloud ice mass, Atmos. Chem. Phys., 14, 12 613–12 629, https://doi.org/10.5194/acp-14-12613-2014, 2014.

Eriksson, P., Ekelund, R., Mendrok, J., Brath, M., Lemke, O., and Buehler, S. A.: A general database of hydrometeor single scattering properties at microwave and sub-millimetre wavelengths, Earth Syst. Sci. Data, 10, 1301–1326, https://doi.org/10.5194/essd-10-1301-2018, 2018.

Eriksson, P., Rydberg, B., Mattioli, V., Thoss, A., Accadia, C., Klein, U., and Buehler, S. A.: Towards an operational Ice Cloud Imager (ICI) retrieval product, Atmos. Meas. Tech., 13, 53–71, https://doi.org/10.5194/amt-13-53-2020, 2020.

Eriksson, P., Emrich, A., Kempe, K., Riesbeck, J., Aljarosha, A., Auriacombe, O., Kugelberg, J., Hekma, E., Albers, R., Murk, A., Møller Pedersen, S., John, L., Stake, J., McEvoy, P., Rydberg, B., Dybbroe, A., Thoss, A., Canestri, A., Accadia, C., Colucci, P., Gherardi, D., and Kangas, V.: The Arctic Weather Satellite radiometer, Atmos. Meas. Tech., 18, 4709–4729, https://doi.org/10.5194/amt-18-4709-2025, 2025.

Eriksson, P., Baró Pérez, A., Müller, N., Hallborn, H., May, E., Brath, M., Buehler, S. A., and Ickes, L.: Advancements and continued challenges in observations and global modelling of atmospheric ice mass, Atmos. Chem. Phys., 26, 2741–2768, https://doi.org/10.5194/acp-26-2741-2026, 2026.

EUMETSAT: MWR-1B-RAD-G [data set], EUMETSAT Data Store, https://data.eumetsat.int/product/EO:EUM:DAT:0905, last access: 14 September 2026, 2024.

Evans, K., Wang, J., O'C Starr, D., Heymsfield, G., Li, L., Tian, L., Lawson, R., Heymsfield, A., and Bansemer, A.: Ice hydrometeor profile retrieval algorithm for high-frequency microwave radiometers: application to the CoSSIR instrument during TC4, Atmos. Meas. Tech., 5, 2277–2306, https://doi.org/10.5194/amt-5-2277-2012, 2012.

Evans, K. F. and Stephens, G. L.: Microwave radiative transfer through clouds composed of realistically shaped ice crystals. Part II. Remote sensing of ice clouds, J. Atmos. Sci., 52, 2058–2072, https://doi.org/10.1175/1520-0469(1995)052<2058:MRTTCC>2.0.CO;2, 1995.

Evans, K. F., Walter, S. J., Heymsfield, A. J., and Deeter, M. N.: Modeling of submillimeter passive remote sensing of cirrus clouds, J. Appl. Meteorol., 37, 184–205, https://doi.org/10.1175/1520-0450(1998)037<0184:MOSPRS>2.0.CO;2, 1998.

Evans, K. F., Walter, S. J., Heymsfield, A. J., and McFarquhar, G. M.: Submillimeter-wave cloud ice radiometer: Simulations of retrieval algorithm performance, J. Geophys. Res., 107, AAC–2, https://doi.org/10.1029/2001JD000709, 2002.

Evans, K. F., Wang, J. R., Racette, P. E., Heymsfield, G., and Li, L.: Ice cloud retrievals and analysis with the compact scanning submillimeter imaging radiometer and the cloud radar system during CRYSTAL FACE, J. Appl. Meteorol., 44, 839–859, https://doi.org/10.1175/JAM2250.1, 2005.

Field, P. R. and Heymsfield, A. J.: Importance of snow to global precipitation, Geophysical Research Letters, 42, 9512–9520, https://doi.org/10.1002/2015GL065497, 2015.

Finnish Meteorological Institute: https://cloudnet.fmi.fi, cloudnet.fmi.fi, accessed: 2026-09-10, 2011.

Fox, S.: An evaluation of radiative transfer simulations of cloudy scenes from a numerical weather prediction model at sub-millimetre frequencies using airborne observations, Radio Sci., 12, 2758, https://doi.org/10.3390/rs12172758, 2020.

Gasiewski, A.: Numerical sensitivity analysis of passive EHF and SMMW channels to tropospheric water vapor, clouds, and precipitation, IEEE T. Geosci. Remote, 30, 859–870, https://doi.org/10.1109/36.175320, 1992.

Gong, J., Wu, D. L., and Eriksson, P.: The first global 883 GHz cloud ice survey: IceCube Level 1 data calibration, processing and analysis, Earth Syst. Sci. Data, 13, 5369–5387, https://doi.org/10.5194/essd-13-5369-2021, 2021.

Hersbach, H., Bell, B., Berrisford, P., Biavati, G., Horányi, A., Muñoz Sabater, J., Nicolas, J., Peubey, C., Radu, R., Rozum, I., Schepers, D., Simmons, A., Soci, C., Dee, D., and Thépaut, J.-N.: ERA5 hourly data on pressure levels from 1940 to present, https://doi.org/10.24381/cds.bd0915c6, 2023a.

Hersbach, H., Bell, B., Berrisford, P., Biavati, G., Horányi, A., Muñoz Sabater, J., Nicolas, J., Peubey, C., Radu, R., Rozum, I., Schepers, D., Simmons, A., Soci, C., Dee, D., and Thépaut, J.-N.: ERA5 hourly data on single levels from 1940 to present, https://doi.org/10.24381/cds.adbb2d47, 2023b.

Holl, G., Eliasson, S., Mendrok, J., and Buehler, S.: SPARE-ICE: Synergistic ice water path from passive operational sensors, J. Geophys. Res., 119, 1504–1523, https://doi.org/10.1002/2013JD020759, 2014.

Intergovernmental Panel on Climate Change (IPCC): Technical Summary, p. 35–144, Cambridge University Press, https://doi.org/10.1017/9781009157896.002, 2023.

Janowiak, J. E., Joyce, R. J., and Yarosh, Y.: A Real-Time Global Half-Hourly Pixel-Resolution Infrared Dataset and Its Applications, Bulletin of the American Meteorological Society, 82, 205 – 218, https://doi.org/10.1175/1520-0477(2001)082<0205:ARTGHH>2.3.CO;2, 2001.

Jimenez, C., Buehler, S. A., Rydberg, B., Eriksson, P., and Evans, K. F.: Performance simulations for a submillimetre wave cloud ice satellite instrument, Q. J. R. Meteorol. Soc., 133, 129–149, https://doi.org/10.1002/qj.134, 2007.

Karlsson, K.-G., Riihelä, A., Trentmann, J., Stengel, M., Solodovnik, I., Meirink, J. F., Devasthale, A., Jääskeläinen, E., Kallio-Myers, V., Eliasson, S., Benas, N., Johansson, E., Stein, D., Finkensieper, S., Håkansson, N., Akkermans, T., Clerbaux, N., Selbach, N., Marc, S., and Hollmann, R.: CLARA-A3: CM SAF cLoud, Albedo and surface RAdiation dataset from AVHRR data - Edition 3 [data set], https://doi.org/10.5676/EUM_SAF_CM/CLARA_AVHRR/V003, last access: 20 February 2026, 2023a.

Karlsson, K.-G., Stengel, M., Meirink, J. F., Riihelä, A., Trentmann, J., Akkermans, T., Stein, D., Devasthale, A., Eliasson, S., Johansson, E., Håkansson, N., Solodovnik, I., Benas, N., Clerbaux, N., Selbach, N., Schröder, M., and Hollmann, R.: CLARA-A3: The third edition of the AVHRR-based CM SAF climate data record on clouds, radiation and surface albedo covering the period 1979 to 2023, Earth System Science Data, 15, 4901–4926, https://doi.org/10.5194/essd-15-4901-2023, 2023b.

Kaur, I., Eriksson, P., Pfreundschuh, S., and Duncan, D. I.: Can machine learning correct microwave humidity radiances for the influence of clouds?, Atmos. Meas. Tech., 14, 2957–2979, https://doi.org/10.5194/amt-14-2957-2021, 2021.

Lauer, A., Bock, L., Hassler, B., Schröder, M., and Stengel, M.: Cloud Climatologies from Global Climate Models—A Comparison of CMIP5 and CMIP6 Models with Satellite Data, Journal of Climate, 36, 281 – 311, https://doi.org/10.1175/JCLI-D-22-0181.1, 2023.

Marshall, J. S. and Palmer, W. M. K.: The Distribution of Raindrops with Size, Journal of Atmospheric Sciences, 5, 165–166, https://doi.org/10.1175/1520-0469(1948)005<0165:TDORWS>2.0.CO;2, 1948.

Mason, S. L., Hogan, R. J., Bozzo, A., and Pounder, N. L.: A unified synergistic retrieval of clouds, aerosols, and precipitation from Earth-CARE: the ACM-CAP product, Atmospheric Measurement Techniques, 16, 3459–3486, https://doi.org/10.5194/amt-16-3459-2023, 2023.

Mattioli, V., Accadia, C., Ackermann, J., Di Michele, S., Hans, I., Schlüssel, P., Colucci, P., and Canestri, A.: The EUMETSAT polar system-second generation (EPS-SG) passive microwave and sub-mm wave missions, in: 2019 PhotonIcs & Electromagnetics Research Symposium-Spring (PIERS-Spring), pp. 3926–3933, IEEE, https://doi.org/10.1109/PIERS-Spring46901.2019.9017822, 2019.

May, E. and Eriksson, P.: The Ice Cloud Imager: retrieval of frozen water mass profiles, Atmos. Meas. Tech., 18, 7243–7266, https://doi.org/10.5194/amt-18-7243-2025, 2025.

May, E., Rydberg, B., Kaur, I., Mattioli, V., H., H., and Eriksson, P.: The Ice Cloud Imager: retrieval of frozen water column properties, Atmos. Meas. Tech., 17, https://doi.org/10.5194/amt-17-5957-2024, 2024.

McEvoy, P., May, E., and Eriksson, P.: CHIP-AWS v1.0.0 2025 archive: Atmospheric ice mass properties [data set], https://doi.org/10.71870/v9dx-rm43, 2026.

Miao, J., Rose, T., Kunzi, K., and Zimmermann, P.: A Future Millimeter/Sub–Millimeter Radiometer for Satellite Observation of Ice Clouds, Int. J. Inf. Millim. Waves, 23, 1159–1170, https://doi.org/10.1023/A:1019655507759, 2002.

Miao, J., Johnsen, K.-P., Buehler, S., and Kokhanovsky, A.: The potential of polarization measurements from space at mm and sub-mm wavelengths for determining cirrus cloud parameters, Atmos. Chem. Phys., 3, 39–48, https://doi.org/10.5194/acp-3-39-2003, 2003.

Nakajima, T. and King, M. D.: Determination of the Optical Thickness and Effective Particle Radius of Clouds from Reflected Solar Radiation Measurements. Part I: Theory, Journal of Atmospheric Sciences, 47, 1878 – 1893, https://doi.org/10.1175/1520-0469(1990)047<1878:DOTOTA>2.0.CO;2, 1990.

Pfreundschuh, S., Eriksson, P., Duncan, D., Rydberg, B., Håkansson, N., and Thoss, A.: A neural network approach to estimating a posteriori distributions of Bayesian retrieval problems, Atmos. Meas. Tech., 11, 4627–4643, https://doi.org/10.5194/amt-11-4627-2018, 2018.

Pfreundschuh, S., Eriksson, P., Buehler, S. A., Brath, M., Duncan, D., Larsson, R., and Ekelund, R.: Synergistic radar and radiometer retrievals of ice hydrometeors, Atmos. Meas. Tech., 13, 4219–4245, https://doi.org/10.5194/amt-13-4219-2020, 2020.

Pfreundschuh, S., Fox, S., Eriksson, P., Duncan, D., Buehler, S. A., Brath, M., Cotton, R., and Ewald, F.: Synergistic radar and sub-millimeter radiometer retrievals of ice hydrometeors in mid-latitude frontal cloud systems, Atmos. Meas. Tech., 15, 677–699, https://doi.org/10.5194/amt-15-677-2022, 2022.

Pfreundschuh, S., Kukulies, J., Amell, A., Hallborn, H., May, E., and Eriksson, P.: The Chalmers Cloud Ice Climatology: A novel robust climate record of frozen cloud hydrometeor concentrations, J. Geophys. Res., 130, e2024JD042 618, https://doi.org/https://doi.org/10.1029/2024JD042618, 2025.

Platnick, S. and M. King, P. H.: MODIS Atmosphere L3 Daily Product, https://doi.org/10.5067/MODIS/MYD08_D3.061, 2017a.

Platnick, S. and M. King, P. H.: MODIS Atmosphere L3 Daily Product, https://doi.org/10.5067/MODIS/MOD08_D3.061, 2017b.

Platnick, S., King, M., Ackerman, S., Menzel, W., Baum, B., Riedi, J., and Frey, R.: The MODIS cloud products: algorithms and examples from Terra, IEEE Transactions on Geoscience and Remote Sensing, 41, 459–473, https://doi.org/10.1109/TGRS.2002.808301, 2003.

Rivoire, L., Marty, R., Carrel-Billiard, T., Chambon, P., Fourrié, N., Audouin, O., Martet, M., Birman, C., Accadia, C., and Ackermann, J.: A global observing-system simulation experiment for the EPS–Sterna microwave constellation, Q. J. R. Meteorol. Soc., 150(762), 2991–3012, https://doi.org/doi.org/10.1002/qj.4747, 2024.

Rydberg, B., Eriksson, P., and Buehler, S. A.: Prediction of cloud ice signatures in submillimetre emission spectra by means of ground-based radar and in situ microphysical data, Quarterly Journal of the Royal Meteorological Society, 133, 151–162, https://doi.org/https://doi.org/10.1002/qj.151, 2007.

Sokol, A. B. and Hartmann, D. L.: Tropical Anvil Clouds: Radiative Driving Toward a Preferred State, Journal of Geophysical Research: Atmospheres, 125, e2020JD033 107, https://doi.org/10.1029/2020JD033107, 2020.

Stephens, G. L., Vane, D. G., Boain, R. J., Mace, G. G., Sassen, K., Wang, Z., Illingworth, A. J., O'connor, E. J., Rossow, W. B., Durden, S. L., et al.: The CloudSat mission and the A-Train: A new dimension of space-based observations of clouds and precipitation, Bull. Amer. Met. Soc., 83, 1771–1790, https://doi.org/10.1175/BAMS-83-12-1771, 2002.

Waliser, D. E., Li, J.-L. F., Woods, C. P., Austin, R. T., Bacmeister, J., Chern, J., Del Genio, A., Jiang, J. H., Kuang, Z., Meng, H., et al.: Cloud ice: A climate model challenge with signs and expectations of progress, J. Geophys. Res., 114, https://doi.org/10.1029/2008JD010015, 2009.

Wang, J., Racette, P., Spinhirne, J., Evans, K., and Hart, W.: Observations of cirrus clouds with airborne MIR, CLS, and MAS during SUCCESS, Geophys. Res. Lett., 25, 1145–1148, https://doi.org/10.1029/97GL03194, 1998.

Wu, D. L., Jiang, J. H., Read, W. G., Austin, R. T., Davis, C. P., Lambert, A., Stephens, G. L., Vane, D. G., and Waters, J. W.: Validation of the Aura MLS cloud ice water content measurements, Journal of Geophysical Research: Atmospheres, 113, https://doi.org/10.1029/2007JD008931, 2008.

Wu, D. L., Gong, J., Deal, W. R., Gaines, W., Cooke, C. M., De Amici, G., Pantina, P., Liu, Y., Yang, P., Eriksson, P., and Bennartz, R.: Remote sensing of ice cloud properties with millimeter and submillimeter-wave polarimetry, IEEE Journal of Microwaves, 4, 847–857, https://doi.org/10.1109/JMW.2024.3487758, 2024.

Yang, Y., Dou, T., Xu, G., Zhou, R., Li, B., Husi, L., Wang, W., and Xiao, C.: FYAI: a Fengyun satellite-based dataset for atmospheric ice water path, Earth Syst. Sci. Data, 18, 1287–1305, https://doi.org/10.5194/essd-18-1287-2026, 2026.